ACS Catalysis

pubs.acs.org/acscatalysis

Research Article

Limited Surface Oxide Growth as a Prerequisite for Stabilizing Low-Loading Iridium Electrodes for PEM Water Electrolysis

Ahyoun Lim, Kahyun Ham, Thomas Quast, Suji Lee, Marc F. Tesch, Steffen Czioska, Daniela Ramermann, Walid Hetaba, Wolfgang Schuhmann, Jan-Dierk Grunwaldt, Sung Ki Cho, Hee-Young Park, Jong Hyun Jang, Sang Hyun Ahn, Ioannis Spanos,* and Hyun S. Park*

Cite This: *ACS Catal.* 2025, 15, 6098−6113

Read Online

ACCESS | Metrics & More | Article Recommendations | Supporting Information

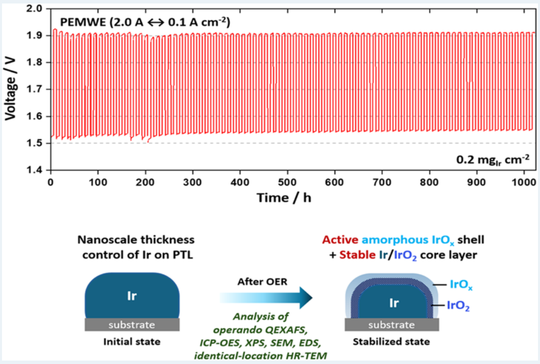

ABSTRACT: As the demand for hydrogen production increases, the economic viability and stability of Ir-based catalysts are crucial in proton exchange membrane water electrolysis (PEMWE). In this study, stable low-loading Ir electrodes (0.2 mg$_{Ir}$ cm^{-2}) with nanometer-thick electrodeposited layers are prepared on Pt-deposited Ti felts. State-of-the-art techniques, such as *operando* quick extended X-ray absorption fine structure spectroscopy (QEXAFS) and identical-location transmission electron microscopy (IL-TEM) employing an ultramicroelectrode (UME), were used to demonstrate the structural transformation of surface Ir during oxygen evolution reaction (OER) and the pivotal role of catalyst film thickness control on the self-terminated growth of crystalline IrO_2, which enhances catalyst stability. A lack of a stabilizing IrO_2 sublayer in thin electrodeposited Ir layers (<10 nm) leads to a fully amorphous catalyst structure, directly impacting its durability. The obtained Ir/IrO_2/IrO_x electrodes achieve catalytic activities of 1.8−12 A mg^{-1} at 1.6 V$_{Cell}$ while maintaining a degradation rate of 8.7 μV h^{-1} @ 2 A cm^{-2} during accelerated stress tests (>1000 h) and 1.6 times greater stability (corresponding to a lifespan of 55,000 h) and 3.6 times higher mass activity compared to commercial Ir oxide electrodes.

KEYWORDS: *proton exchange membrane water electrolysis, oxygen evolution reaction, low-loading iridium electrode, operando X-ray absorption spectroscopy, porous transport electrode*

1. INTRODUCTION

The urgent task of developing decarbonized industries must be accomplished to mitigate the current environmental crisis related to global warming, which is caused by the increased greenhouse gas emissions in the fossil fuel-based economy.[1] In this context, green hydrogen produced via water electrolysis is a promising carbon-free energy carrier with a high energy density (lower heating value: 33.3 kWh kg^{-1}). Among the different electrolysis techniques involving the hydrogen evolution reaction (HER) and oxygen evolution reaction (OER), proton exchange membrane water electrolysis (PEMWE) has many advantages, such as high efficiency, compact design, quick start-up, pressurized hydrogen production, and wide load range. However, the limited selection of material components, such as expensive noble iridium-based OER catalysts, which are required to achieve sufficient stability under harsh acidic conditions at high-current loads, remains a prominent challenge for reducing the PEMWE capital cost. Surmounting these obstacles and scaling up the commercial PEMWE process depend on the enhanced utilization efficiency of Ir in OER catalysis.[2]

Several strategies have been proposed to produce efficient and durable OER electrodes with reduced Ir contents. For instance, Park et al. reported an Ir-based electrode with an inverse opal structure electrode, current density of 0.9 A cm^{-2} at 1.6 V$_{Cell}$, and loading of only 0.02 mg$_{Ir}$ cm^{-2} for enhanced mass transport in OER catalysis.[3] Kim et al. described a three-dimensional (3D) electrode with a woodpile structure consisting of Ir nanowires, which exhibited not only high surface areas but also facile mass transport through a controlled void volume, resulting in a high activity of 0.4 A cm^{-2} at 1.6 V$_{Cell}$ and a loading of 0.01 mg$_{Ir}$ cm^{-2}.[4] Oh et al. fabricated self-supported Ir electrodes through the galvanic replacement of an electrodeposited Ni support with Ir, which demonstrated an activity of 0.4 A cm^{-2} at 1.6 V$_{Cell}$ and a loading of 0.05 mg$_{Ir}$ cm^{-2}. However, none of these highly efficient electrodes with extremely low Ir loading demonstrated stable operation for more than 50 h at current densities higher than 1.0 A cm^{-2} in

Received: December 20, 2024
Revised: March 21, 2025
Accepted: March 24, 2025
Published: March 31, 2025

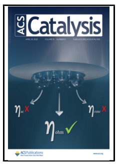

https://doi.org/10.1021/acscatal.4c07864
ACS Catal. 2025, 15, 6098−6113

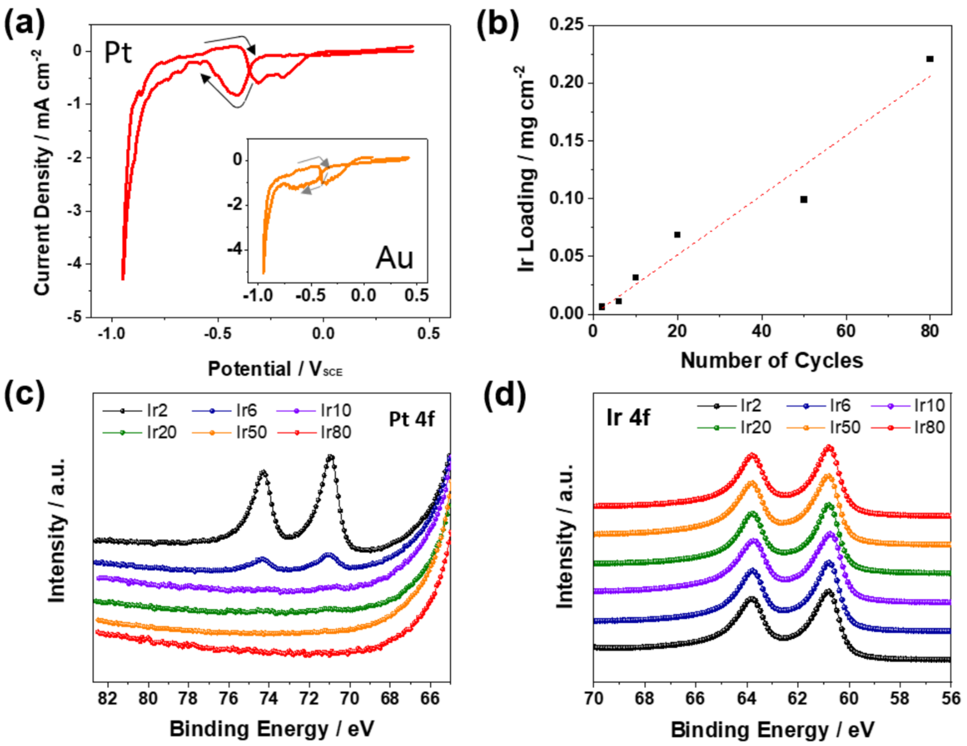

Figure 1. (a) CV profiles (scan rate: 5 mV s^{-1}) recorded during a single cycle of Ir electrodeposition on a Pt disk electrode (inset: an Au disk electrode) without rotation. (b) Electrodeposited Ir amounts on a Ti-felt porous transport layer determined via ICP−OES. XPS profiles of the (c) Pt and (d) Ir $4f_{7/2}$ and $4f_{5/2}$ states obtained at different number of electrodeposition cycles (2, 6, 10, 20, 50, and 80).

PEMWE.[3−6] The degradation rate of the low-Ir anode was often unacceptably high during practical operation, e.g., 15 mV h^{-1} at 1.0 A cm^{-2} during 12 h of operation for the electrode with an Ir loading of 0.05 mg_{Ir} cm^{-2}.[5]

The stability of OER catalysts and electrodes is affected by multiple factors, such as the crystallinity and chemical stability of the catalysts, the physical strength of agglomerated catalytic nanoparticles (NPs),[7−11] degradation of catalyst layer binders,[10,12] and deterioration of catalyst−porous transport layer (PTL) interfaces,[13−15] in the continuous PEMWE process. Most stable OER electrodes for PEMWE contain thick catalyst layers composed of large amounts of Ir NPs exceeding 1.5 mg_{Ir} cm^{-2}.[16−24] The thick and porous catalyst layer[25,26] contains longer discharge pathways for the chemically dissolved and physically detached IrO_x catalysts, which allows the redeposition and encapsulation of the catalyst within the active catalyst layer.[27] This makes the high Ir loading on the anode surface a possible reason for the stable PEMWE process.[24] It also implies that a high utilization efficiency of the precious catalyst can be achieved at the initial PEMWE stage using low-loading Ir electrodes; however, the utilization efficiency is quickly and significantly reduced during long-term operation owing to the limited stability of low-loading Ir anodes. For example, approximately 50% of the performance loss was reported for an Ir electrode with a low loading of 0.1 mg_{Ir} cm^{-2} after 23,000 potential cycles from 1.45 to 2.0 V_{Cell} (ca. 383 h) during the single cell operation, whereas the degradation rate of a commercial device with an Ir loading of 1−2 mg_{Ir} cm^{-2} was less than few tens of μV h^{-1}, which corresponded to a lifetime of 40,000−80,000 h.[11]

Herein, to overcome challenges that prevent high mass activity and stability of OER anodes, ultrathin Ir layers of nanoscale thickness were sequentially electrodeposited on previously Pt-coated Ti PTL electrodes through a simple sequential electrochemical method developed by Ahn et al. in 2015.[28] However, for the first time, this electrochemical method is used to prepare low-loading Ir electrodes used in PEMWE. The controlled thickness of the deposited Ir catalyst makes these catalysts ideal for ex situ and *operando* investigation of their structural characteristics, activity, and stability during OER to better understand the structure transformation dynamics of Ir-based electrocatalysts for PEMWE. The iridium structure transformation was monitored *operando* via quick extended X-ray absorption fine structure (QEXAFS) spectroscopy and compared to amorphous IrO_x and crystalline iridium metal powder catalysts up to potentials of 1.8 $V_{RHE,\ reversible\ hydrogen\ electrode}$ in a 3-electrode configuration. X-ray photoelectron spectroscopy (XPS), inductively coupled plasma optical emission spectroscopy (ICP−OES), and identical-location transmission electron microscopy (IL−TEM) on Ir-loaded ultramicroelectrodes (UMEs) were performed to investigate the layer-by-layer structure, revealing a self-terminated growth of catalytically active IrO_x and IrO_2 layers on the metallic Ir surface of the PEMWE anode. This was further complemented by accelerated stress test operation for more than 1000 h without compromising the high activity of the PEMWE catalysts.

2. RESULTS AND DISCUSSION

2.1. Electrode Fabrication and Ex Situ Characterization. Pt particles were first electrodeposited on a Ti PTL as a catalyst support to achieve high conductivity and electrochemical surface area (ECSA) for the OER catalysis, followed by the electrodeposition of Ir shells on Pt particles (details of this procedure are provided in the Section 4). The applied potentials for Ir electrodeposition were accurately determined

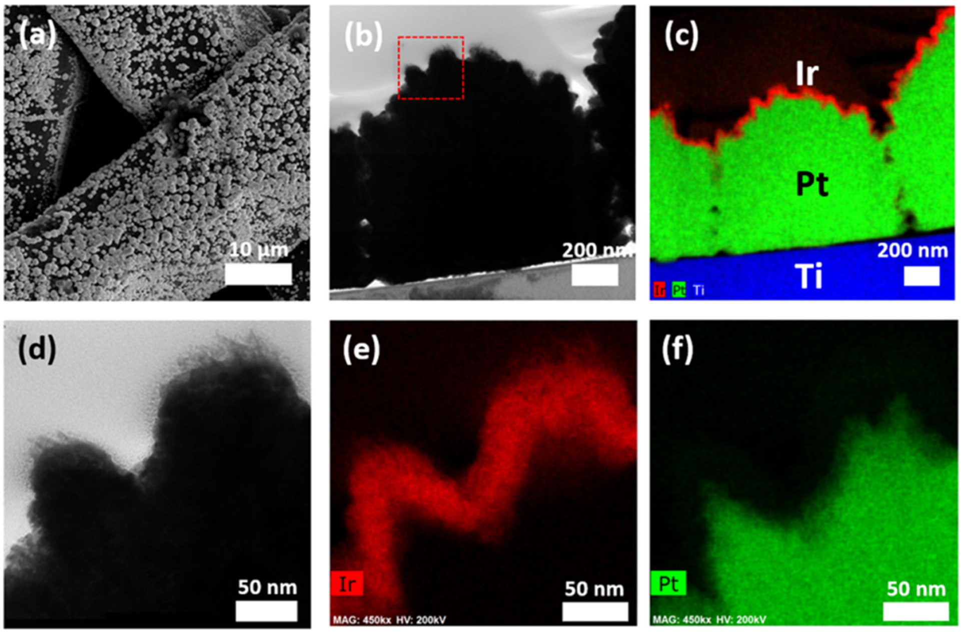

Figure 2. (a) FE−SEM image of Ir20/Pt on a Ti-felt PTL (Ir20/Pt/Ti). (b) TEM image and (c) elemental map of the Ir20/Pt/Ti cross section obtained after FIB cutting. (d) Enlarged TEM image of the marked range in panel (b) and its EDS (e) Ir and (f) Pt maps.

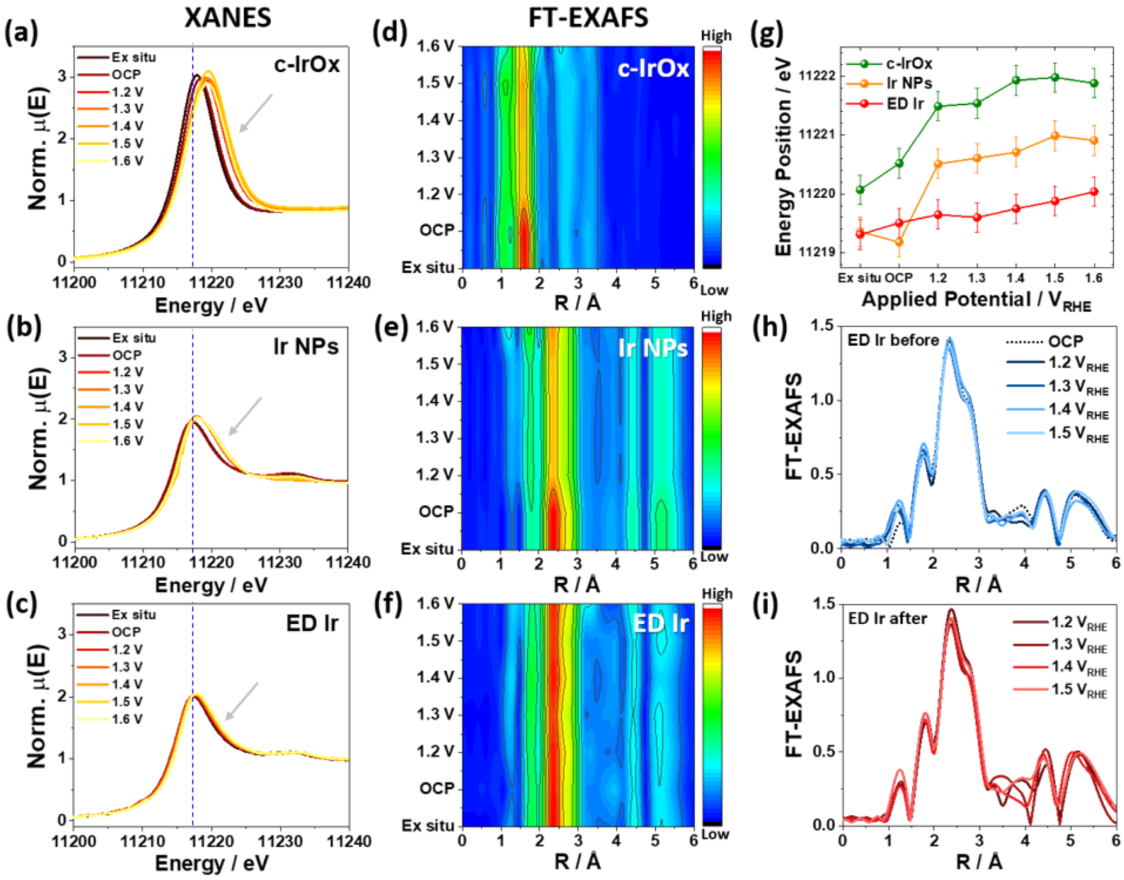

Figure 3. XANES spectra for (a) commercial IrO_x NPs (c-IrO_x), (b) Ir metal NPs, and (c) electrodeposited Ir (ED Ir) at the OCP, 1.2, 1.3, 1.4, 1.5, and 1.6 V_{RHE} complemented by an ex situ spectrum recorded in air before assembling the cell (dashed blue line serves as a guide to the eye for the white line shift). Panels (d−f) show contour plots of the k^2-weighted Fourier transformed *operando* QEXAFS spectra of the respective catalysts at the denoted potentials. The color code indicates the relative intensities of the FT-EXAFS. Panel (g) shows the energy position of the falling edge inflection point indicated by the gray arrows in panels (a−c) of the white line features for all catalysts and conditions (cf. Figure S6) with an estimated error of ± 250 meV. (h) Fourier transformed EXAFS spectra of ED Ir obtained at 1.2, 1.3, 1.4, and 1.5 V_{RHE} before (additionally including the initial OCP state) and (i) after 6 h of chronoamperometric (CA) operation at 1.8 V_{RHE}.

to control the amount of the deposited catalyst on a well-defined Pt disc electrode in a separate experiment. Cyclic voltammetry (CV) experiments conducted on a Pt disk electrode in an Ir precursor solution[28] (pH = 4, Figure 1a) revealed that the reduction current of Ir(III) started to flow from −0.30 $V_{SCE,\ standard\ calomel\ electrode}$ (0.18 V_{RHE}) with a peak current at −0.40 V_{SCE} (0.08 V_{RHE}). This reduction was rapidly decreased and ultimately quenched at negative potentials lower than −0.55 V_{SCE} (−0.07 V_{RHE}) as the electrode surface was passivated by the adsorbed protons for the HER, as reported by Ahn et al.[28] The reduction reaction of Ir(III) can be reactivated after proton desorption by applying sufficiently high positive potentials to the electrode. A similar CV profile was observed on the Au disk electrode (inset, Figure 1a). During electrode preparation, a controlled amount of metallic Ir was deposited on the Pt/Ti PTL surface by conducting square wave voltammetry (SWV) for the Ir(III) reduction−proton desorption reactions. Specifically, a single SWV cycle consisted of three potentials at 0.40 V_{SCE} (0.88 V_{RHE}) for the rest stage, −0.65 V_{SCE} (−0.17 V_{RHE}) for Ir(III) reduction, and 0.0 V_{SCE} (0.48 V_{RHE}) for proton desorption with durations of 2, 10, and 2 s, respectively (Figure S1).[28] In the repeated SWV cycles, the amount of Ir loading on the Pt/Ti−TPL surface was maintained at an average value of 2.7 μg cm^{-2} per cycle, as determined via ICP−OES (see Section 4 and Figure 1b). For instance, an Ir amount of 220 μg cm^{-2} was deposited after 80 cycles. Hereafter, the electrodes are named according to the number of deposition cycles applied during preparation; for example, Ir20 denotes the electrode subjected to 20 SWV cycles of Ir(III) reduction, and ED Ir describes the electrochemically prepared catalyst.

XPS analysis was performed to identify the chemical states of the thin Ir catalysts formed on Pt/Ti PTLs with different thicknesses. For Ir2, two distinct peaks detected at 71.0 and 74.3 eV were assigned to the binding energies of the $4f_{7/2}$ and $4f_{5/2}$ states of metallic Pt, respectively (Figure 1c). As the amount of electrodeposited Ir increased to Ir10, the intensity of the peak obtained for the area underneath the metallic Pt layer in the Ir/Pt/Ti PTL decreased. This indicates that the Ir layer in Ir10 was thicker than the maximum probing depth of XPS, i.e., approximately 4−5 nm (Al Kα radiation);[29] therefore, the Ir layer fully covered the Pt layer in Ir10. As reported previously, the self-terminating electrodeposition method produces compact Ir layers with controlled thicknesses at nanometer resolution. The $4f_{7/2}$ and $4f_{5/2}$ states of metallic Ir with XPS peaks at 60.8 and 63.8 eV, respectively, were detected for all electrodes from Ir2 to Ir80, yielding visually identical spectra, as expected for the reductive electrodeposition of Ir (Figure 1d).

The morphology of the Ir layers in Pt/Ti PTL was confirmed through electron microscopy (Figures 2a, S2, and S3(a)−(c)). The cross-sectional image of catalyst particles in Ir20 revealed the Ir layer with a thickness of approximately 30 nm covering the 0.5−1.5 μm Pt particles on the Ti PTL (see the field emission scanning electron microscopy (FE−SEM) and focused ion beam (FIB)−TEM/energy-dispersive X-ray spectroscopy (EDS) images presented in Figure 2).[30] The Ir film on the Pt support was actually an agglomerated layer composed of small Ir NPs with sizes of 2−4 nm (Figure S3(d)). However, the electrochemically deposited thin film of Ir NPs was connected to the Pt microparticle interlayer, which differed from the standard porous catalyst layer with a micrometer thickness incorporating ionomers fabricated by a spray or decal process.[25]

2.2. *Operando* XAS Studies.

Detailed insights into the Ir structure and its changes during the OER at the atomic level were obtained using *operando* QEXAFS spectroscopy. X-ray absorption near-edge structure (XANES) and extended X-ray absorption fine structure (EXAFS) measurements were performed at the Ir L_3-edge (Figure 3). In previous studies, XANES and EXAFS were, e.g., utilized to explain the OER activity of Ir by relating it to the Ir oxidation state and Ir−Ir (Ir−O) bond length.[31−33] Importantly, in contrast to XPS, XAS in the hard X-ray regime has a probing depth in the micrometer range (the attenuation length across the Ir L_3-edge is 2−5 μm).[34] Therefore, the hard X-ray spectra reflect the entire structure, comprising surface and bulk phases. This means, in case of surface oxidation of a compact film with a low surface-to-bulk ratio, the spectra will be dominated by the not oxidized bulk, while systems with a high surface-to-bulk ratio, such as nanoparticles, can be expected to yield a clear response in the spectra when the surface is oxidized.[35] As discussed before, the electrodeposited Ir layers possess the characteristics of a compact layer composed of agglomerated nanoparticles. Therefore, the *operando* QEXAFS measurements can shed light on how this catalyst structure affects the ED Ir oxidation behavior.

The experiments were performed using a specially designed hard X-ray transmission flow cell (Figure S4)[36] and the QEXAFS setup at beamline P64 in PETRA III.[37,38] Au-coated Kapton tape was used as the working electrode to support the Ir catalyst (details are provided in the Section 4) instead of Ti felt to acquire a sufficiently strong Ir transmittance signal and inhibit a pinhole effect, which can lead to spectrum distortion. First, the catalyst layer was analyzed under open-circuit potential (OCP) conditions. Subsequently, 1.2 V_{RHE} was applied and iteratively increased to 1.6 V_{RHE} in 0.1 V increments. Compared with conventional XAS experiments, in which the collection of a single spectrum can take several minutes, the QEXAFS mode enables a significantly shorter detection time. In this study, a single spectrum was collected across the Ir L_3 edge in 0.5 s, together with the Pt L_3 edge of a Pt reference foil for energy calibration. A collection time of 10 min per potential yielded 1200 single spectra. By averaging these spectra, the signal-to-noise level was improved, and, more importantly, the distortions of individual spectra caused by evolving O_2 gas bubbles at high anodic potentials during *operando* experiments were averaged out.[39]

Prior to the *operando* experiments, the initial states of commercial Ir oxide NPs (c-IrO_x), Ir metal NPs (Ir NPs), and ED Ir were compared under ex situ conditions. The XANES spectra of c-IrO_x exhibit a notably higher white line intensity as compared with those of Ir NPs and ED Ir, indicating a lower 5d orbital occupancy related to the Ir oxidation state around Ir(III) and Ir(IV) (Figures 3a−c and S5(a)).[40,41] In addition, the white line position of c-IrO_x (ca. 11218 eV) is positively shifted compared to Ir NPs and ED Ir (ca. 11214 eV), as would be expected for Ir in a higher oxidation state.[42] The ex situ EXAFS spectra recorded for the three catalysts show that only IrO_x NPs exhibit a predominant first-shell Ir−O feature around R = 1.6 Å, while Ir NPs and ED Ir show a strong peak at around R = 2.5 Å related to the first Ir shell (Figures 3d−f and S5(b)). The broad peaks in the R-scale at 4.5 and 5.5 Å obtained for Ir NPs and the ED Ir indicate the second and third shells of Ir atoms. This corroborates the XPS results,

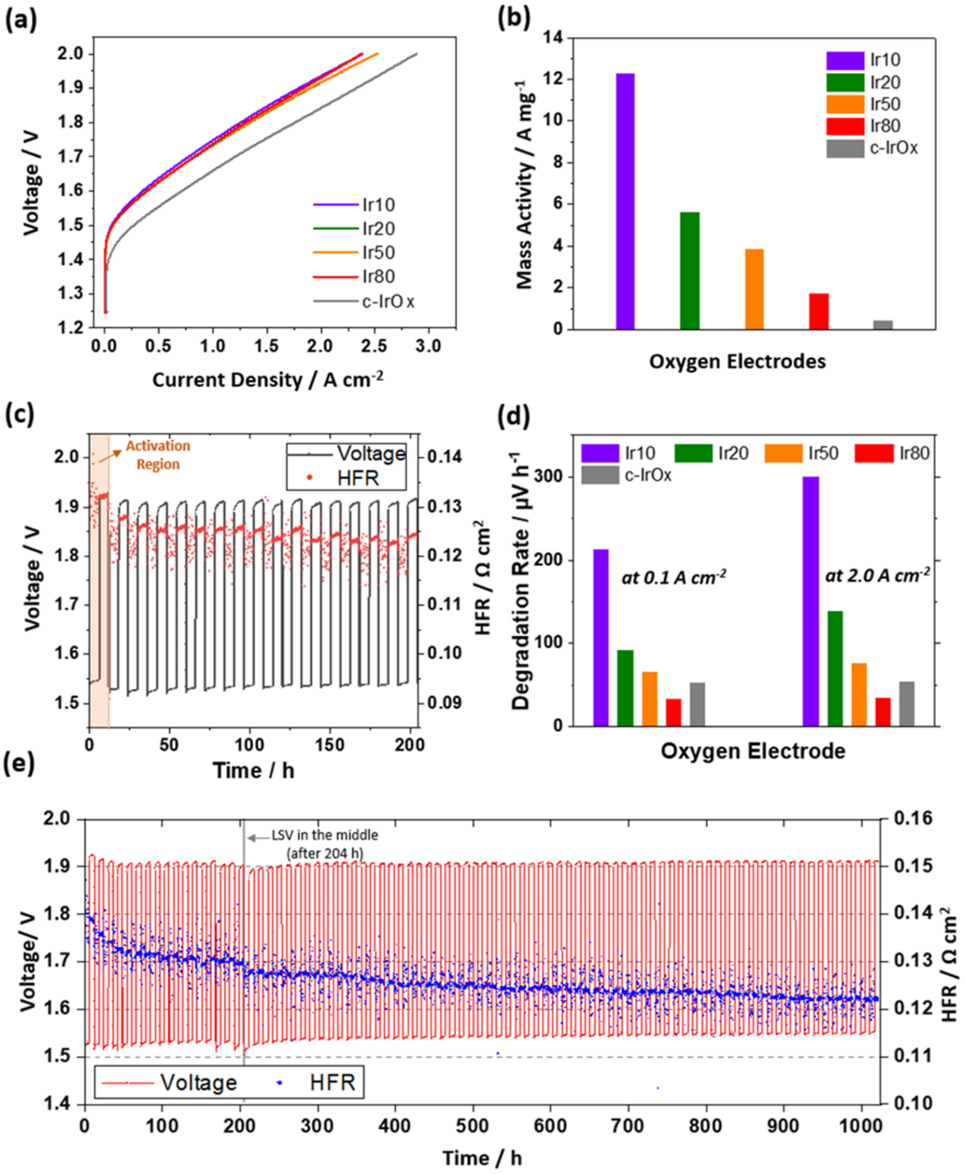

Figure 4. (a) *IV* curves of the fabricated anodes recorded during the PEMWE. (b) Mass activities measured for different anodes during PEMWE at 1.6 V. (c) Cell voltages and HFRs (10 kHz) of Ir20 obtained at 0.1 and 2.0 A cm^{-2} during 204 h of operation. (d) Degradation rates of different anodes measured at 0.1 and 2.0 A cm^{-2} during the long-term PEMWE operation (*iR*-corrected voltage, 204 h, except for Ir80, which operated for 1020 h). (e) Cell voltages and HFRs (10 kHz) of Ir80 measured during 1020 h of operation.

indicating that ED Ir was composed of an Ir metallic phase similar to that of Ir NPs.

To investigate changes in the catalyst structure as compared to the ex situ state upon increasing the potential from the OCP to the OER conditions, *operando* XAS experiments were performed, and the obtained XANES and EXAFS spectra were compared for all specimens. In the *operando* XANES (Figures 3a–c and S6 a,c,e), clear shifts in the white line position with increasing applied potential were observed for all Ir catalysts owing to the Ir oxidation reaction (Figure S6(g)).[43,44] The white line shift appears most pronounced for the c-IrO$_x$; however, also the Ir NPs show a clear shift of the white line of almost 1 eV, indicating that a discernible fraction of the Ir NP is oxidized. In both catalysts, the change in the white line position is most pronounced upon application of the first potential step. On the other hand, the shift in the white line of ED Ir appeared smaller, even when the first potential step was applied, indicating that the ED Ir maintained an overall lower Ir oxidation state. These potential induced changes in the XANES spectra, related to the catalyst oxidation, become even clearer when plotting the energy position of the white line falling edge inflection point (Figure 3g), showing the same trends. Finally, the spectral feature in the energy region from ca. 11225–11255 eV also appears more affected by the applied potential for the Ir NP, compared to the ED Ir, with the latter appearing almost unaffected when applying increasing potential steps. To obtain more information about the coordination geometry, an additional EXAFS analysis was performed. *operando* EXAFS spectra are displayed as contour maps in Figure 3d–f, in which the intensities are distinguished by color (from blue = low to red = high). Upon applying more positive potentials, c-IrO$_x$ underwent a reduction of the Ir–O bond length (d = 2.01 Å → 1.96 Å, Tables S2–S4) owing to the change in the oxygen environment according to the OER mechanism.[32] Ir(III) species in c-IrO_x are partially oxidized to Ir(IV) when the potential changes from OCP to 1.2 V_{RHE}, and they are expected to further oxidize to Ir(V) species or form coordinatively unsaturated metal sites on the surface such as μ_1-O species above 1.2 V_{RHE} (1.2 → 1.6 V_{RHE}).[45−47] This may contribute to the continuous reduction of the Ir−O bond length when approaching the OER relevant potentials. The *operando* EXAFS spectrum of Ir NPs (Figure 3e) shows two distinctive changes: (1) a significant decay of the Ir−Ir peak (R = 2.4 Å) intensity upon the application of potentials and (2) the formation of a broad feature at $R < 2.0$ Å that is related to the Ir−O bond length[48] at positive potentials, especially at 1.6 V_{RHE}. Interestingly, ED Ir (Figure 3f) exhibits a more stable Ir−Ir peak as compared with that of Ir NPs regardless of the applied potential, showing a peak intensity comparable to that acquired under the OCP condition, whereas Ir NPs demonstrate an abrupt change when 1.2 V_{RHE} is applied instead of the OCP.

To elucidate this discrepancy between Ir NPs and ED Ir in more detail, the coordination numbers of the Ir−Ir (CN_{Ir-Ir}) and Ir−O (CN_{Ir-O}) bonds were determined as functions of the applied potential (Figure S6(h)) for all three catalyst types. Note again that these data represent an average over the catalyst surface and the bulk. In the case of c-IrO_x, the material retained the CN_{Ir-O} of around 6 despite its distorted amorphous structure with reduced Ir(III) species, which was attributed to the rutile motif that inherently possessed an IrO_6 coordination geometry. For Ir NPs and ED Ir, on the other hand, both materials exhibit a simultaneous decrease in CN_{Ir-Ir} and increase in CN_{Ir-O} with increasing potential up to 1.6 V_{RHE}, suggesting the formation of Ir oxide. This is consistent with the results of other studies, in which Ir oxide was detected on the Ir metal surface near the OER potential.[43,44,49,50] However, ED Ir shows only minor changes in CN_{Ir-O}, suggesting that a minimal fraction of the catalyst surface is oxidized. Figure S6(h) indicates that ED Ir maintains higher CN_{Ir-Ir} and lower CN_{Ir-O} values compared with those of Ir NPs. It has to be noted that since the ED Ir appears to predominantly maintain its initial structure, indicating only a small fraction to be redox active, a quantitative analysis of the bulk-dominated EXAFS signal with respect to changes in Ir−Ir or Ir−O distances at the surface would be too speculative at this point. As discussed above, the different morphologies of the two catalyst layers can be attributed to the different degrees of oxidation in Ir NPs and ED Ir, which likely originate from the different dispersions of catalyst particles on the Ti PTL surface. Importantly, this strongly indicates that the catalyst NPs of ED Ir form an electrochemically bonded compact thin film, in which the oxidation process is restricted to the film surface, whereas Ir NPs form a porous catalyst layer with a higher extent of surface exposure to water and its oxidation.

Finally, *operando* EXAFS spectra were recorded at different potentials up to 1.5 V_{RHE} after 6 h of operation at 1.8 V_{RHE} to obtain more information on the structural stability of ED Ir (Figure 3h,i). During the stability test, the Ir−O bond feature (R < 2.0 Å)[48] was more pronounced owing to the highly oxidative environment; however, the first Ir−Ir shell at R = 2.4 Å was maintained (Figure S7). After the stability test, the EXAFS intensity assigned to Ir−O increased slightly; however, the first Ir−Ir shell was surprisingly dominant without losing its intensity even after 6 h of operation in 0.1 M H_2SO_4 (Figure 3i and Table S5). Unlike the Ir NPs, the stable Ir−Ir peak observed in the case of ED Ir may serve as a key factor contributing to the overall stability. Based on these findings, it was concluded that ED Ir formed a stable and compact layer that maintained its metallic nature even throughout prolonged electrochemical measurements. However, the topmost surface layers participate in the OER. Thus, we anticipate that surface oxidation takes place only at the topmost layers, activating the OER for the ED Ir and keeping the Ir sublayer itself stable.

Analyzing the electrode in a PEM cell after long-term operation would contribute to a better understanding of degradation phenomena in a single cell. However, the direct analysis of Ir/Pt/Ti electrodes is not facile for several reasons. First, when using Ti substrates, Ir transmission signals cannot be adequately obtained and pinhole effects could disturb obtained spectra. Second, analyzing an Ir/Pt/Ti electrode reveals overlapping regions of Pt and Ir signals in EXAFS analysis, complicating the analysis of the Ir spectra.

The degradation and dissolution rates of catalysts in half-cell operation are orders of magnitude faster than those in single cell operation.[51] Therefore, we believe that the results obtained from 6 h of long-term operation in a half-cell configuration can provide meaningful data and insights into elucidating the behavior observed during hundreds or thousands of hours of operation in a single cell configuration.

2.3. Evaluation of Performance and Durability of PEMWE Catalysts.

The initial performances of the different ED Ir electrodes after 10−80 deposition cycles during single cell operation (Figure S8) were practically identical regardless of the electrodeposited Ir amount (Figure 4a). Accordingly, the utilization efficiency of the catalysts increased with decreasing layer thickness, increasing the mass activity from Ir80 to Ir10 by approximately a factor of 7 at the beginning of the PEMWE operation (Figure 4b). Although the estimated ECSA of Ir80 (calculated from H_{UPD} in PEMWE, details in the Section 4) was 3.6 times higher than that of Ir10, the apparent performances of Ir80 and Ir10 were similar. It was hypothesized that mass transport-related phenomena due to high oxygen production and inefficient electrolyte transport through the inner Ir80 layers blocked significant parts of the Ir active sites during OER.[52] c-IrO_x also exhibited higher single cell performance than that of ED Ir with an approximately 0.1 V lower onset voltage at around 1.35 V_{Cell} as compared with the value of 1.45 V_{Cell} obtained for ED Ir.[49] However, the ED Ir electrodes demonstrated significantly higher catalyst utilization efficiency, i.e., mass activities of 12.3 and 1.8 A mg^{-1} at 1.6 V_{Cell} for Ir10 and Ir80, respectively, compared to the 0.5 A mg^{-1} for the c-IrO_x, due to the 7−48 times lower Ir amount in ED Ir compared to c-IrO_x.

In order to understand the effect of electrodeposited Pt on Ir performance, 0.07−0.08 mg_{Ir} cm^{-2} of commercial Ir catalyst was spray-coated on two Ti-felt electrodes with (denoted as ED-Pt/Ti) and without Pt (denoted as pristine-Ti), since the ED Ir cannot be deposited directly on the Ti felt.[28] The lower R_{ct} and R_{ohm} values of the ED-Pt/Ti electrode compared to the pristine-Ti measured by electrochemical impedance spectroscopy (EIS) indicated that the ED-Pt/Ti electrode has a higher surface area compared to the pristine-Ti and improved interfacial contact between the spray-coated Ir catalyst and the Ti substrate (Figure S9). Furthermore, the 4.7 and 2.9 times lower ohmic and charge transfer resistance of ED Ir, respectively, were observed at 1.5 V when compared to commercial Ir under similar low Ir loading conditions (0.07 to 0.08 mg_{Ir} cm^{-2}, Figure S10). The enhanced ionic/electrical conductivity of the catalyst layer and the high utilization

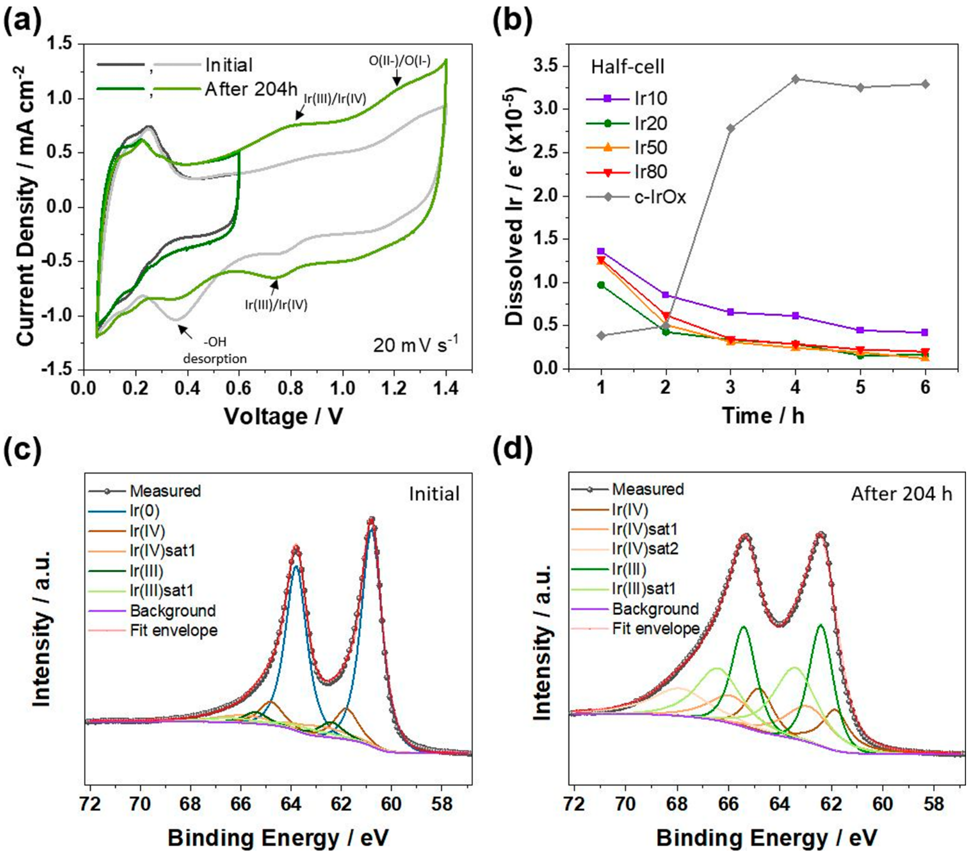

Figure 5. (a) Cyclic voltammograms (scan rate: 20 mV s^{-1}) of Ir20 recorded before and after long-term operation. Fully humidified N_2 and H_2 gases were purged at the anode and the cathode, respectively. (b) Dissolved Ir amounts measured every 1 h during 6 h of operation at 1.6 and 1.9 $V_{pseudo-RHE}$. XPS profiles of the Ir $4f_{7/2}$ and $4f_{5/2}$ states recorded for Ir20 (c) before and (d) after 204 h of long-term PEMWE operation.

efficiency of the Ir ED catalyst, even at low Ir concentration without ionomers, were primarily due to the evenly distributed nm scale thin Ir layer without agglomeration and better contact between the catalyst active sites and the membrane. Although Pt is recognized as being active for the OER, the probability of its direct participation in the OER or its influence on the intrinsic OER activity of Ir is minimal due to the coverage (Figure 1c) and thickness (Figure 2e) of Ir on Pt (details in the Supporting Information).

To investigate the catalyst stability, current swing operations with high and low current densities were employed as a long-term operation protocol (>200 h) to simulate the fluctuating operating conditions of industrial green hydrogen production. To achieve a low current density during long-term measurements, the open-circuit voltage (OCV) condition was deliberately excluded to avoid unintended polymer degradation from the excess hydroxyl radical formation by the permeated hydrogen and oxygen species near the equilibrium potentials of water electrolysis.[53,54] Rakousky et al. also reported that the dynamic operation mitigated the performance loss from the ohmic resistance (R_{ohm}); however, catalytic degradation was clearly induced by the high-current operation at 2 A cm^{-2} around 1.9 V_{Cell} as compared with the moderate operation at 1 A cm^{-2}.[19] In this context, dynamic measurements were conducted at 0.1 A cm^{-2} (6 h) and 2 A cm^{-2} (6 h) to investigate the stability of the Ir electrodes, including short chronopotentiometry measurements performed between 2 and 0.1 A cm^{-2} for 17 s (details are provided in the Section 4). In addition, thicker membranes (including N115) were selected to avoid membrane failure during the long-term operation of the PEMWE catalysts, although higher device performance can be achieved by using thinner membranes with lower ion transport resistances (Figure S10).

At the beginning of the long-term stability measurements, both the ohmic and kinetic resistances decreased, as indicated by comparing the average cell voltages for 0−6 and 12−18 h of operation (Figures 4c and S11). The ohmic resistance (R_{ohm}), i.e., the high-frequency resistance (HFR) at 10 kHz measured every 10 min during operation, decreased from 0.14 to 0.12−0.13 Ω cm^2 at 2.0 A cm^{-2}, which was likely caused by the thinning or activation of membranes for all samples.[12,55] Considering that there is no ionomer in the ED Ir electrodes in this study and previous studies reported a reduction in membrane thickness at a rate of 15−25 nm h^{-1} during electrolysis operations, the observed ohmic loss during long-term operation due to membrane thinning is considered plausible.[56,57] Interestingly, catalyst activation was also observed for the ED Ir electrodes during the initial operation with a decrease in the kinetic overvoltage, i.e., approximately 16 mV at 0.1 A cm^{-2}. Because oxidation catalysts in electrochemistry are usually activated through surface oxidation, including the OER at the IrO_x electrode with *OH or *OOH adsorption, the gradual oxidation of the Ir surface of the ED Ir electrodes was attributed to the initial voltage decrease in this study, consistent with the results of previous EXAFS investigations.[49] Activation of the ED Ir electrodes was observed even after 204 h of operation (or 1020 h of operation for Ir80), except for Ir10, which contained the lowest amount of Ir among the ED Ir electrodes, for both the apparent and *iR*-corrected *I*−*V* curves (Figure S12). As a result, the initial catalyst activation compensated for the voltage increase caused by other degradation processes during the long-term operation of the ED Ir electrodes. However, initial activation was not observed for c-IrO_x because the surface was fully oxidized from the beginning of the measurement process. The average increase rates of the apparent cell voltage obtained at 0.1 and 2.0 A cm^{-2} for each separate 6 h period of the current swing operation were 1.3 ± 0.7 and 3.8 ± 1.5 mV h^{-1}, respectively. In the 6 h short-current steps, significant reversible degradation was dominant during the device operation, which prohibited the long-time operation. However, by repeated changes of the operating current, the fluid stream of the electrodes can be perturbed to discharge the trapped gas bubbles, and the cell voltage can be recovered at the beginning of the next operation cycle (Figure 4c). Suermann et al. reported similar results in their dynamic protocol for the low and high current densities (1 ↔ 4 A cm^{-2}).[19,23]

The durability of the different electrodes was evaluated by the variance in the *iR*-corrected cell voltage after 12 h of operation, thereby excluding the effects of initial electrode activation or reduction in R_{ohm} during the long-term current swing operation (Figure S11(c)). In general, an inverted relationship between the mass activity of the OER catalyst and stability was established by comparing the degradation rates of the ED Ir electrodes with different catalyst loadings (Figure 4b−d). This also implies that the stability of the ED Ir electrode can be closely related to the thickness of the reductively prepared Ir film on the electrode surface, as concluded from the similar apparent PEMWE performances; the ECSA is less affected by the Ir loading, whereas the film thickness can be increased with increasing Ir usage. However, significant degradation rates of 93 and 139 μV h^{-1} were observed for Ir20 at 0.1 and 2.0 A cm^{-2}, respectively, whereas Ir80 exhibited a significantly lower degradation rate of 34 ± 1 μV h^{-1} at 2.0 A cm^{-2}. The stability of Ir80 was even higher than that of c-IrO_x, which corresponded to a degradation rate of 54 ± 1 μV h^{-1} at 2.0 A cm^{-2}.

The lower degradation rate of Ir80 than that of c-IrO_x was particularly interesting, considering the higher cell voltage of Ir80 than that of c-IrO_x; the *iR*-corrected voltages applied to Ir80 and c-IrO_x were approximately 1.65 and 1.57 V_{Cell} at 2.0 A cm^{-2}, respectively (discussion in Supporting Information, Figures 4e and S11). The inverse relationship between the amount of Ir used and electrode stability was also not applicable to Ir80 and c-IrO_x, as the Ir loading of the more stable Ir80 electrode was 6.8 times lower than that of c-IrO_x. The apparent stability of Ir80 before applying an *iR* correction was even higher than the *iR*-corrected stability because the reduced R_{ohm} due to membrane thinning partially compensated for the PEMWE catalytic degradation in the long-term operation.[12] For instance, an apparent degradation rate of 8.7 μV h^{-1} obtained for Ir80 at 2.0 A cm^{-2} was calculated over a period from 12 to 1020 h during stability testing, considering the R_{ohm} decrease of 9.8% observed after 1000 h of measurements. In other words, the lifespan of Ir80 until reaching 2.4 V_{Cell} at 2.0 A cm^{-2} can be extrapolated to 55,000 h (≈6.3 years) if only the catalyst degradation rate obtained for the initial 1000 h period is maintained for several years without other significant stack failures.

2.4. Ir Catalyst State after OER.

To verify the high stability of the ED Ir electrodes during long-term operation, their surface state and material dissolution were characterized via CV, linear sweep voltammetry (LSV), XPS, and ICP−OES before and after 204 h of PEMWE (Figure 5). For the CV and LSV measurements conducted during PEMWE, a Pt-coated cathode was used as a pseudoreference electrode (pseudo-RHE) purged with fully humidified H_2 gas, while the ED Ir electrodes were examined. During the measurements, no significant membrane degradation or gas crossover was observed (Figure S13).

Starting with Ir20, the double-layer capacitance and pseudocapacitive Ir(III)/Ir(IV) redox peaks developed in the CV curves owing to the surface Ir oxidation after 204 h of the stability test (Figure 5a). Distinct H_{UPD} peaks between 0.05 and 0.6 $V_{pseudo\text{-}RHE}$ were detected after the stability test, indicating the presence of metallic Ir exposed during long-term operation (Figure 5a).[9] The observed increase in the double-layer capacitance and reduction of H_{UPD} peaks implied that the ED Ir surfaces were roughened, while metallic Ir oxidized to IrO_x in the long-term stability test. Ir(III/IV) and O(II−/I−) redox peaks were also clearly observed at around 0.75 and 1.25 $V_{pseudo\text{-}RHE}$ in Figure 5a.[9,46,58] The reduction peak of Ir20 developed around 0.35 $V_{pseudo\text{-}RHE}$ was detected only after CV scanning to 1.4 V and was not observed when the CV curve was vortexed at the 1.1 $V_{pseudo\text{-}RHE}$ upper limit (Figures 5a and S14). The reduction peak at 0.35 $V_{pseudo\text{-}RHE}$ developed after changing the CV scan window can be attributed to the desorption of adsorbates (possibly hydroxyl ions), which are adsorbed at the IrO_x electrode in the 1.1−1.4 $V_{pseudo\text{-}RHE}$ scan window. The desorption current at 0.35 $V_{pseudo\text{-}RHE}$ also decreased after the long-term stability test; therefore, the adsorbed hydroxyl density on the ED Ir surfaces decreased along with surface oxidation in the prolonged OER reactions. The desorption peak potential and hydroxyl binding energy were not significantly changed during the stability test.

The O 1s spectra recorded by XPS further corroborated the increased amounts of μ1-O(H) and μ_2-O(H) species on the surface after operation (Figure S15(a)−(c)). μ_1-O(H) and μ_2-O(H) species, including hydroxyl coverage, were previously suggested as an OER activity descriptor (details in the Supporting Information).[46,47,59−61] The obtained CV curves and O 1s XPS analysis results confirm that ED−Ir possesses highly conductive surfaces with facile hydroxyl adsorption/desorption processes. However, for c-IrO_x, the H_{UPD}, Ir(III)/Ir(IV) redox and hydroxyl peaks were not clearly visible in the CV curves owing to the low conductivity and high capacitive current of the oxide films even before the stability test (Figure S14(a)).

To further elucidate the catalyst stability, the amount of Ir dissolved from the electrodes during the OER was quantified in a half-cell configuration. To replicate the operational conditions of PEMWE devices, the electrode potential of ED Ir and c-IrO_x was repeatably switched between 1.6 and 1.9 V_{RHE} every 15 min during 6 h of operation. The surface oxidation of ED Ir was confirmed via high-angle annular dark-field scanning transmission electron microscopy (HAADF−STEM) and EDS mapping after the operation (Figure S16). For the ICP−OES results, a discernible trend was observed, wherein the dissolution rate of ED Ir decreased over time for all electrodes, ultimately reaching a constant level corresponding to an Ir/e^- ratio of 1.2−2.0 × 10^{-6} for Ir20 to Ir80 and approximately 3.3 × 10^{-5} of Ir/e^- for c-IrO_x (Figure 5b). The

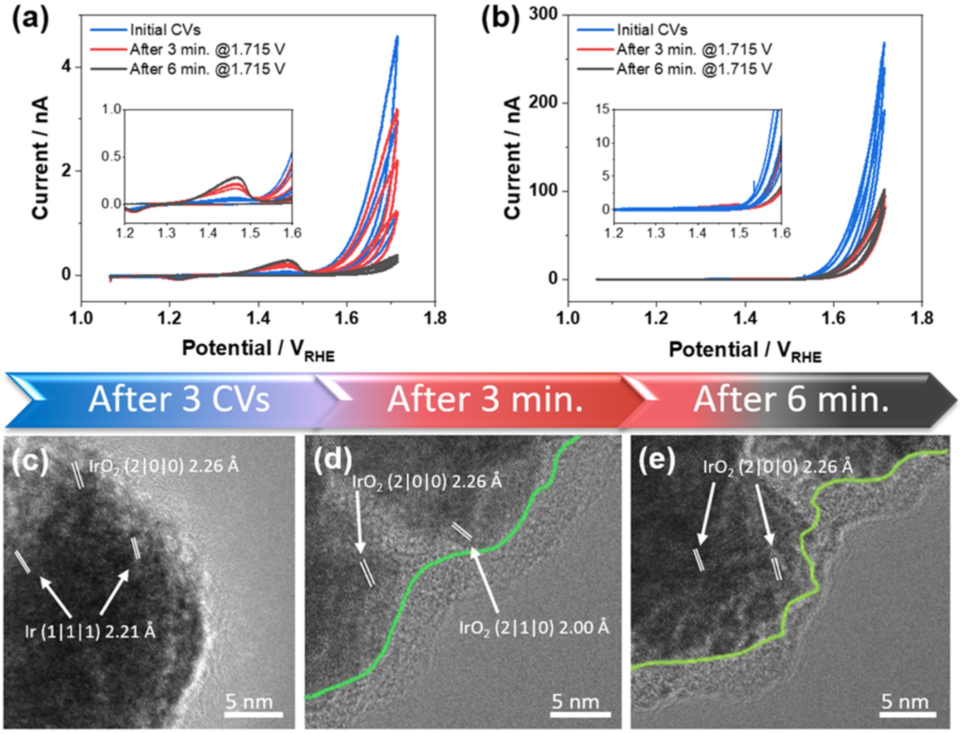

Figure 6. Cyclic voltammograms of the (a) Ir10 and (b) Ir20 Au@CNE UMEs. Measurements were performed in a 0.1 M H_2SO_4 solution at a scan rate of 10 mV s^{-1} using an Ag/AgCl 3 M KCl electrode as the reference/counter electrode. HR−TEM images of the Ir50 Au@CNE UME obtained at different stages of the applied electrochemical stress after the (c) initial 3 CV cycles, (d) 3 min, and (e) 6 min at an applied potential of 1.715 V_{RHE}. The green line indicates the border between the amorphous IrO_x species on the surface and the crystalline IrO_2 phase.

twice as high Ir dissolution rate of Ir10 as compared with those of the other ED Ir electrodes with thicker Ir films may be due to the loss of the metallic Ir support and the physical integrity of the film during the OER (see Section 2.5). From the ICP−OES results, it was concluded that there is a critical Ir layer thickness, which is necessary to maintain the stability of ED Ir. We relate this to the necessity for a remaining metallic sublayer unaffected by surface oxidation.[49,62−64] In contrast, the c-IrO_x electrode exhibited a rapid increase in the Ir degradation rate, which subsequently stabilized at levels 15−30 times higher than those of the ED Ir electrodes, confirming the effect of the robust film structure on the stability of the OER electrode (Figure 5b).

The XPS profiles of pristine Ir20 contain two main photoemission peaks at 60.8 eV (Ir(0) $4f_{7/2}$) and 63.8 eV (Ir(0) $4f_{5/2}$) (Figure 5c). However, after the durability test, the Ir 4f core level spectrum exhibited an overall shift of 1.5 eV toward higher binding energies and an asymmetric line shape, indicating surface oxidation into a mixture of Ir(III) and Ir(IV) (Figure 5d and Table S1). In comparison to the *operando* XANES measurements, which suggested no significant oxidation on average across the complete catalyst, this indicated the oxidation clearly detectable by XPS is limited to the very surface of the catalyst layer (<10 nm). The formation of the surface oxide layer in single cell operation was further elucidated by TEM and electron energy loss spectroscopy (EELS). It was observed that oxide layer formation on a catalyst coated Ti felt, operated for 120 h at 3 mA/cm^{-2}, was restricted to a surface layer in the range of approximately 6 nm, while the rest of the Ir film retained its metallic character. This is in alignment with ex situ XPS results as well as with operando results obtained with hard X-ray spectroscopy in a half-cell configuration. This is discussed in more detail in the Supporting Information (Figure S15(d)−(g)). The high ratio of the Ir(III) state compared to the Ir(IV) state under ex situ conditions following the electrolysis operation indicates that the surface of Ir oxide is amorphous, composed of primarily electrophilic μ_1−OH and μ_2−OH, while also suggesting that the oxidation state is flexible (details of peak positions in the Supporting Information). Recently, Lee et al. investigated the effects of the mixed oxidation states of layered Ir/IrO_x catalysts on the OER activity and stability for PEMWE.[63] In this study, the higher Ir(III) ratio of the IrO_x catalysts exerted a positive effect on their activity but adversely affected the stability with material dissolution, whereas the higher Ir(IV) ratio resulted in higher durability but lower activity. By minimizing the Ir(III) exposure on the surface with Ir(IV) and maintaining the average oxidation state of 2.98 for the Ir/IrO_x catalysts, a trade-off relationship between the activity and stability of the OER catalysts was partially avoided; the Ir/IrO_x catalyst contained approximately 43% of Ir(IV) on the surface, which corresponded to [Ir(IV)]/[Ir(III) + Ir(IV)] = ∼41% (Table S1).[63] In other words, for the ED Ir catalysts consisting of the surface oxide and subsurface metallic layers with the balanced Ir(III) and Ir(IV) species, the dissolution process was minimized without compromising the OER activity.

2.5. TEM Analysis of the Ir Catalyst Transformation during OER.

To corroborate the previous findings and to better understand the previously observed changes in the crystal structure of the deposited Ir layer, depending on electrochemical stress and ICP−OES data, an ultramicroelectrode (UME)-based analysis was performed. According to Figure S17, the unit structure of ED Ir was loaded at the UME to investigate the Ir crystal structure at different stages of the

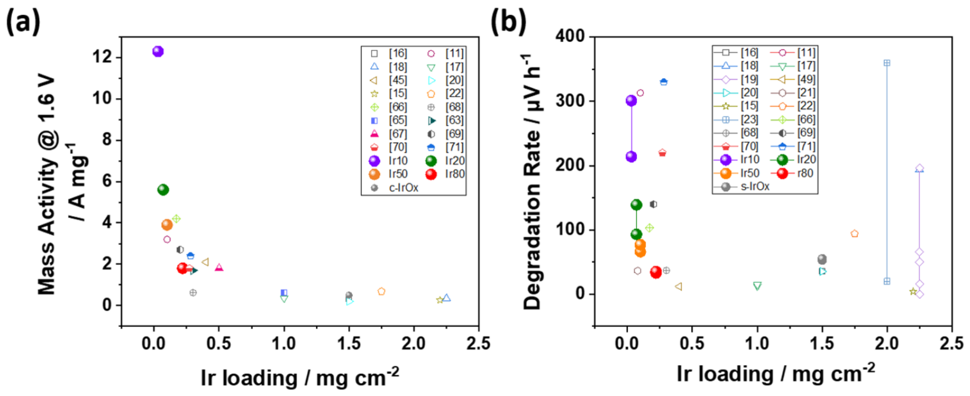

Figure 7. (a) Mass activities at 1.6 V and (b) degradation rates measured at various Ir loadings during the long-term PEMWE operation in this and previous studies. The degradation rates were calculated based on the *iR*-corrected voltages in this work and voltages without *iR*-corrections in the other studies.

OER process via identical-location HR−TEM. In this approach, carbon nanoelectrodes (CNEs) were used as the UME platform to load micrometer-sized Au particles as the support for ED Ir (for more details, see Figure S17). Due to the fact that Pt tends to grow in thick, rounded layers on CNEs due to its tendency to agglomerate, it becomes challenging to perform HR-TEM analysis, as the overlapped layers may obscure the image. For this reason, Au was used instead (Figure S18), which we expect to have no significant impact on the electrochemistry applied and the resulting reaction mechanisms investigated (further discussion in Supporting Information, Part V. Identical Location TEM Analysis). Subsequently, the procedure employed for depositing different amounts of Ir onto the Au surface, corresponding to 10, 20, and 50 deposition cycles (Figure S19), was used.

TEM results demonstrated that 10 deposition cycles led to the formation of a thin Ir film on the Au@CNE UME surface with a thickness of 2−4 nm (Figure S20(a)−(c)). In contrast, after 20 Ir deposition cycles, a significantly higher Ir amount was deposited, indicating dendritic growth (Figure S20(d)−(f)). The prepared electrodes were electrochemically tested, as shown by the CV responses of the Ir10/Ir20 Au@CNE UMEs (Figure 6a,b); the results of CA measurements conducted between CV series are displayed in Figure S21. The Ir10 Au@CNE UME exhibited not only a lower initial current but also a faster activity decay as compared with those of the Ir20 Au@CNE UME. The rapid decay in activity is attributed to the dissolution of Ir from the Au surface, which can be directly observed by SEM (Figure S22) and verified by the larger Au redox peaks obtained for the increasingly accessible Au surface during the repeated CV measurements (Figure 6a). The Ir20 Au@CNE UME also revealed the initial loss of activity; however, no large redox features of the underlying Au layer were detected during the repeated CV measurements. These results support the ICP−OES data obtained for the stable IrO_x layers of the thicker ED Ir electrodes (Figure 5b). The STEM image of the Ir20 Au@CNE UME demonstrates fewer changes in the Ir structure than the STEM image of the Ir10 Au@CNE UME (Figure S23(a,b)). Using HR−TEM (Figure S23(c,d)), the amorphization of the crystal surface with an amorphous layer thickness of approximately 2−5 nm was observed, and only lattice spacings from IrO_2 were detected in the near-surface region of the Ir20 Au@CNE UME.

To investigate the evolution of the amorphous layer and crystal structure, the prepared Ir50 Au@CNE UME was exposed to different levels of electrochemical stress (Figure S24), and HR−TEM images were obtained between different steps. Figure 6c shows the HR−TEM image of the Ir50 Au@CNE UME subjected to three CV cycles up to 1.715 V_{RHE} (Figure S24(a)). The crystal lattice spacing of IrO_2 was detected close to the surface; however, the Ir crystal lattice spacings were still visible, indicating limited changes in the crystal structure induced by CV. After 1.715 V_{RHE} was applied for 3 min, the obtained HR−TEM image (Figure 6d) reveals the presence of an amorphous layer on the Ir50 Au@CNE UME surface along with the crystal lattice spacings of IrO_2, indicating a fully oxidized catalyst surface. After applying another 3 CV cycles, the structure is slightly decayed but still stable, as evidenced by the OER current (Figure S24(b)). After 1.715 V_{RHE} was applied for another 3 min, the corresponding identical-location HR−TEM image shows stabilization of the amorphous region (Figures 6e and S24(b,d)). In Figure S25(b), the corresponding EDS elemental analysis of the HR−TEM region (Figure S25(a)) indicates a slight enrichment of oxygen on the surface. The amorphization and oxygen enrichment of the near-surface oxide observed (Figure S25(c)−(d)) are in good agreement with the QEXAFS findings, where limited ED Ir oxidation was observed (Figure 3). The stabilized thickness of the amorphous layer after the OER matches the Ir thickness of Ir10, which can explain why a thin layer of Ir10 was significantly less stable than the thicker Ir layers of the ED Ir electrodes (it lacks underlying metallic Ir and crystalline IrO_2 layers, which stabilize the amorphous region and thereby the catalytically active surface). Although the catalyst growth during Ir electrodeposition and dissolution depends on the substrate and type of operation, the UME data demonstrate that the Ir/IrO_2 sublayer formed beneath the amorphous Ir oxide layer with a certain thickness is the main factor affecting the stability of the OER catalysts; therefore, the control over the Ir thickness is important for maintaining the catalyst stability.

2.6. States of Ir/Ir Oxide Catalysts for PEMWE.

In Figure 7 and Table S6, the results of this study are compared with the previously reported data, which were obtained by performing long-term electrolysis tests to investigate the mass activity of Ir catalysts and plotting the device degradation rate during PEMWE as a function of the Ir loading.[11,15−23,49,63,65−71] In general, device stability is enhanced with increasing Ir loading. For instance, Rakousky et al. demonstrated a highly stable PEMWE process with a degradation rate of 12 μV h^{-1} and high Ir loading of 2.25 mg cm^{-2}.[18] On the contrary, the PEMWE conducted using highly conductive and efficient nanoporous Ir nanosheets with an Ir loading of only 0.06 mg cm^{-2} resulted in a degradation rate of approximately 100 μV h^{-1} and limited 200 h of operation.[66] A stable operation (degradation rate: <25 μV h^{-1}) for 1000 h was achieved at an Ir loading of 0.4 mg$_{\text{Ir}}$ cm^{-2} by Siracusano et al.; however, the operation current density was moderate (1 A cm^{-2}), and no data at high current densities were obtained.[49] Yu et al. successfully fabricated an efficient IrO$_x$/Nafion catalyst layer via reactive spray deposition with an Ir loading of only 0.08 mg$_{\text{Ir}}$ cm^{-2} during PEMWE operation, demonstrating both high performance and stability with a degradation rate of 36.5 μV h^{-1}.[21] However, the effect of R_{ohm} changes on the device stability remains unclear. In this study, variations of R$_{\text{ohm}}$ were also considered via HFR measurements during stability tests (Figure 4), and degradation rates were calculated based on *iR*-corrected voltage to focus on the electrode degradation (Figure 7b).

In ED Ir electrodes, both the activity and stability of the PEMWE catalysts were maximized at a minimum Ir loading of 0.2 mg$_{\text{Ir}}$ cm^{-2} (Figure 7).[11,63] While the trade-off relationship between the activity and stability of the ED Ir OER electrodes was established, all electrodes investigated in this work contained relatively low Ir amounts ranging from 0.03 (Ir10) to 0.2 (Ir80) mg$_{\text{Ir}}$ cm^{-2}. No degradation in the PEMWE performance was observed during LSV measurements conducted after 204 h (or 1020 h for Ir80) of stability testing when the active IrO$_x$ catalyst was formed on the reductively prepared Ir films with thicknesses larger than 30 nm (Figure S12). For Ir80, the device operated steadily with an apparent degradation rate of 8.7 μV h^{-1} at 2 A cm^{-2} during 1020 h of the current swing operation, corresponding to a lifespan of 55,000 h. Importantly, the amount of Ir used per power consumption was approximately 0.06 g$_{\text{Ir}}$/kW at 2 A cm^{-2}, which was 8–9 times lower than those of commercial PEMWE devices.[72] The degradation rate of Ir80 determined without considering the effect of R_{ohm} reduction on the long-time stability was only 35 μV h^{-1}, with a mass activity 3.6 times higher than that of c-IrO$_x$.

3. CONCLUSIONS

This study highlights the critical importance of controlling the thickness and compactness of a low-loading iridium thin-film catalyst layer prepared via a simple sequential electrodeposition method of Pt and Ir on Ti felt for ensuring the stability in PEMWE. The prepared ultrathin Ir catalyst layers were investigated *operando* and demonstrated high mass activity and durability during long-term operation for PEMWE. Strong binding between the Pt-deposited Ti PTL and Ir catalyst layer, achieved without additional ionomers, significantly enhances the electrical conductivity and utilization efficiency of the Ir catalysts during the OER at ultralow Ir loadings. The *operando* QEXAFS data obtained at the Ir L$_3$-edge, alongside the ex situ XPS profiles of the O 1s and Ir 4f$_{7/2}$ and 4f$_{5/2}$ states, confirmed only a surface oxidation of the ED Ir catalyst without changing the coordination environment of Ir sublayers. Importantly, the identical-location HR–TEM analysis of the Ir UMEs further revealed the formation of a stabilized and self-terminated amorphous IrO$_x$ layer (2–5 nm) on top of the crystalline Ir/IrO$_2$ sublayers following the OER operation. These results underscore that crystalline Ir/IrO$_2$ sublayers are critical for maintaining catalyst stability, while the high OER activity is attributed to a thin amorphous IrO$_x$ surface layer. It was shown that precise control of the Ir thickness, particularly at loadings exceeding 30 nm in thickness, is crucial. A balanced oxidation state of (Ir(III)/Ir(IV)) of the top Ir layers was observed via XPS after the long-term PEMWE operation, including the formation of crystalline IrO$_2$ layers between the Ir sublayer and top IrO$_x$ layer during the OER. The limited growth of IrO$_x$ on the ED Ir surface promoted catalyst stabilization, as indicated by the reduced dissolution of Ir detected by ICP–OES without compromising the OER. Additionally, the mass activity was 4–25 times higher than that of c-IrO$_x$ used as the PEMWE anode, while a high device stability corresponding to a degradation rate of just 8.7 μV h^{-1} was reached at 2 A cm^{-2} for >1000 h of operation. We demonstrate that the produced low-loading Ir thin-film electrodes are sufficiently stable for commercialization without the use of ionomer. A limitation of electrodeposition is its restricted applicability to the continuous fabrication process of electrodes, as it often requires a batch process, which can be slow for the mass production of large electrodes. Compared to existing low-loading electrodes, our focus has primarily been on stability. By elucidating the phenomenon of the Ir/IrO$_2$/IrO$_x$ structure transformation and stabilization during the OER within the Ir film layers, through *operando* QEXAFS and identical-location TEM analysis, we were able to identify the conditions necessary for achieving stable Ir catalyst layers devoid of ionomers. We believe this electrodeposition technique can be used for fundamental research as the thickness of the catalyst layer can be easily controlled and observed on the nm scale.

Our work breaks the general concept of the instability for low-loading catalysts during PEMWE. The feasibility of manufacturing highly efficient and stable Ir catalyst layers enables the mass production and commercialization of PEMWE catalysts via their microscale loading on the oxygen electrode.

4. METHODS AND MATERIALS

4.1. Electrodeposition. In the first step, the Ti PTL (250 μm, Bekaert) was electrochemically coated with Pt. The precursor solution consisted of H$_2$PtCl$_6$ (20 mM, >99.9%, Sigma–Aldrich) in an H$_2$SO$_4$ solution (0.5 M). The Ti PTL was immersed in C$_2$H$_2$O$_4$ (5 wt %, oxalic acid, DAEJUNG) at 65 °C for 30 min to remove an oxide layer from the surface and rinsed with deionized water. Subsequently, the Ti PTL was immersed into the precursor solution, and a potential was applied to the reaction system to maintain the current density of − 10 mA cm^{-2} (galvanostatic approach) for 5 min to electrodeposit Pt (~0.37 mg$_{\text{Pt}}$ cm^{-2}).[30] For this purpose, a three-electrode setup was used with Ti mesh and a saturated calomel electrode (SCE) serving as the counter and reference electrodes, respectively. In this Pt electrodeposition process, the Pt(IV)Cl$_6^{2-}$ complex was reduced to Pt(II)Cl$_4^{2-}$ complex (1) and then to Pt(II)Cl$_4^{2-}$ complex to obtain metallic Pt as the final product (5).

$$\mathrm{Pt(IV)Cl_6^{2-} + 2e^- \rightleftarrows Pt(II)Cl_4^{2-} + 2Cl^-} \quad E° = 0.68\ \mathrm{V_{SHE}} \tag{1}$$

$$\mathrm{Pt(0)-Cl^- + Pt(II)Cl_4^{2-} + 2e^- \rightleftarrows Pt(0)-Pt(0)-Cl^- + 4Cl^-} \quad E° = 0.76\ \mathrm{V_{SHE}} \tag{2}$$

Ir was deposited on the prepared Pt/Ti substrates via a pulsed electrodeposition sequence: 0.4 V_{SCE} (2 s) → −0.65 V_{SCE} (10 s) → 0.0 V_{SCE} (2 s) as one cycle in the Ir precursor solution at 70 °C. The Ir precursor solution was composed of K_3IrCl_6 (3 mmol), Na_2SO_4 (0.5 M), and H_2SO_4, adjusting the pH to 4.[28] The amount and thickness of the Ir layer were controlled by increasing the number of electrodeposition cycles from 2 to 80.

4.2. Physicochemical Characterization. XPS (Thermo Fisher, Al K-α) was utilized to characterize surface chemical compositions and oxidation states. FE−SEM and EDS employing a Teneo VolumeScope scanning electron microscope (Thermo Fisher) were used to analyze the sample morphology and catalyst distribution on the electrode surface. Cross-sectional examinations of the ED Ir catalysts were performed using TEM (Thermo Fisher Talos) after preparing vertical cuts by an FIB. The amounts of Pt and Ir in the electrodeposited catalysts were determined via ICP−OES (Optima 7300DV&Avio500, PerkinElmer). Samples were treated in aqua regia, a microwave digestion system, and sequentially diluted in 6 wt % hydrochloric acid before the ICP−OES analysis as a pretreatment.

4.3. Operando QEXAFS. XANES and EXAFS measurements were performed at the P64 beamline of the PETRA III storage ring at the DESY, Hamburg, utilizing a QEXAFS setup. For the *operando* measurements, an electrochemical flow cell setup designed by Binninger et al. was used.[36] The electrode was composed of an Au-coated Kapton tape (containing a 100 nm Au layer on a 55 μm Kapton support) serving as a working electrode, a carbon paper (TGP-H-060, Toray) used as a counter electrode, and an Ag|AgCl reference electrode (for a representative sketch, see Figure S4). The ED Ir layer was directly electrodeposited onto the Au-coated Kapton tape. To achieve a sufficiently high Ir thickness for absorption, 160 electrodeposition cycles were performed. Ir NPs and c-IrO_x were loaded onto the Au-coated Kapton tape by spray coating a thin layer from a slurry comprising the catalyst, a Nafion ionomer solution (10 wt % with respect to the catalyst amount), and ethanol. The loadings were 1.2 mg cm^{-2} for Ir NPs and 1.0 mg cm^{-2} for c-IrO_x. The electrolyte used in the experiments was 0.1 M of H_2SO_4 applied in a continuous flow at a rate of 5 mL min^{-1} using a peristaltic pump. The total detection time of the averaged X-ray spectrum was 10 min at each potential (1.2 to 1.6 V_{RHE}), including the OCP for Ir NPs and c-IrO_x and 20 min for ED Ir160. The QEXAFS technique allowed the collection of two full spectra in the energy range from 11.0 to 12.2 keV per second (monochromator oscillation frequency: 1 Hz), resulting in 1200 (2400 for ED Ir160) spectra at each applied potential. All spectra were collected in the transmission mode utilizing an ionization chamber. A piece of Pt foil for energy calibration (Pt L_3-edge at 11543 eV) was installed in the downstream path of the beam and measured during transmission simultaneously to each Ir spectrum with a second ionization chamber. Individual samples and reference spectra were processed with the program JAQ.[73] The average spectra were calculated from the extracted individual spectra using a Python script. Energy calibration was performed with the *Athena* application of the software package *Demeter*[74] using the second derivative of the spectra to align the energy of the Pt reference foil. The XANES and EXAFS data were also extracted by *Athena*. For normalization and background removal from absorption spectra, the pre-edge was in a range from −150 to −30 eV relative to E^0 of Ir L_3 edge, and the postedge was from 150 to 680 eV relative to E^0. To prevent signal interference from the Au substrate, we restricted the postedge range to values below 680 eV. The *k*-weight is 2. EXAFS interpretation was conducted by using the *Artemis* application of the *Demeter* software package. Ex situ measurements of the samples were performed in transmission mode for 10 s, and the obtained results were analyzed according to a previously described procedure. To get the initial EXAFS fitting parameter, standard chemicals such as Ir black and IrO_2 (Rutile structure) from Sigma-Aldrich were utilized. The EXAFS fitting parameters are described in Tables S2−S5.

For the short-term stability test, a constant potential of 1.8 V_{RHE} over a period of 6 h was applied. To track changes in the Ir structure, seven *operando* QEXAFS spectra were acquired during the stability test at 1.8 V_{RHE} while averaging every 30 min to enhance the signal-to-noise ratio. In addition, spectra were obtained from 1.2 to 1.5 V_{RHE} (in 0.1 V_{RHE} intervals) for 20 min at each potential after completing the stability test (further discussion in Supporting Information, Part V. Identical Location TEM Analysis: Preparation of Ir films with different thicknesses).

4.4. Electron Energy Loss Spectroscopy. The EELS map and corresponding spectra were acquired on a Thermo Fisher Talos F200X TEM using a Gatan Continuum S spectrometer. The TEM was operated at 200 kV acceleration voltage, and EELS maps were generated from spectrum images recorded using an energy dispersion of 1.5 eV to include the Ti $L_{2,3}$, O K, and Ir $M_{4,5}$ edges in one spectrum. The EEL spectra for investigation of the fine structure of the Ti $L_{2,3}$ and the O K edge were recorded using an energy dispersion of 0.15 eV, leading to an energy resolution of 1.2 eV.

4.5. Quantification of Dissolved Catalysts in Half-Cells. The electrochemical measurements were performed for each ED Ir/Pt/Ti electrode at potentials of 1.6 and 1.9 V_{RHE} in an H_2SO_4 solution (0.1 M, 120 mL). Pt wire and an Ag|AgCl electrode were used as the counter and reference electrodes, respectively. Repetitive and sequential operations for 15 min at each potential (1.6 and 1.9 V_{RHE}) were performed for 6 h. Every 1 h, 12 mL of the solution was extracted from the reactor and stored in a test tube, and 12 mL of the fresh H_2SO_4 solution (0.1 M) was added to the reactor to replenish the extracted electrolyte. The amount of Ir dissolved in 12 mL of the extracted solution was measured by using a SpectroBlue ICP−OES instrument (Ametek).

4.6. Analysis of Ir Catalysts on CNEs. *4.6.1. Preparation of CNEs.* To prepare the CNEs, quartz capillaries (inner diameter: 0.9 mm; outer diameter: 1.2 mm) were pulled using a P-2000 laser puller (Sutter Instruments) at the following parameters: heat: 740; filament: 4; velocity: 45; delay: 130; pull: 100. The obtained nanocapillaries were filled with carbon using a fully automatized setup to obtain the CNEs, as reported earlier.[75] The nanometer-sized tips of the capillaries were inserted into a ceramic capillary under an argon counter flow (AirLiquide, 99.999%) of 50 mL min^{-1}. The capillaries were filled with a carbon precursor (1 bar of butane (AirLiquide, 99.5%) and propane (3 bar, AirLiquide, technical grade)), which was thermally decomposed to yield a conductive carbon film covering the inside of the capillary. The heating coil was moved twice along the CNE by using a computer. In this process, a two-step temperature profile was used, where a peak temperature of 990 ± 5 °C was reached in the first step, followed by a second step with a peak temperature of 800 ± 5 °C, followed by a 35 s cooldown period to 450 ± 5 °C until the heating coil was switched off. The as-obtained CNEs were subsequently processed inside the SEM instrument using a Ga^+ ion-based FIB, resulting in the disk-shaped CNEs.

4.6.2. Preparation of CNE-Based Au Electrodes. An electrochemical deposition approach was used to prepare the CNE-based Au electrodes. The FIB-processed CNEs were slightly recessed by exposing the tips to 650 °C in air for 5−10 s, thereby burning the excess carbon and creating a recession depth up to 4 μm (at a duration of 10 s), as shown in Figure S17(a). A nanoelectrode recession was made to enhance the stability of the Au deposition on the carbon surface because the Au deposit was additionally stabilized inside the conical quartz capillary. Au was electrodeposited onto the recessed CNE by immersing the CNE into a 10 mM $H[AuCl_4]$ solution (Sigma−Aldrich) and then applying a constant potential of 0.7 V vs Ag/AgCl/3 M KCl while monitoring the current (Figure S17(b)). The observed current during Au deposition followed a well-defined trend in which most of the Au precursor was consumed inside the cavity, decreasing the reduction current. Subsequently, the current stabilized for a short time because of the limited diffusion of the precursor inside the cavity. Afterward, the current increased while the deposited Au layer grew toward the capillary opening, owing to the reduced diffusion length. Finally, the slope of the current increased after reaching the capillary opening, while the Au layer was constantly increasing its size during spherical growth. The Au deposition stopped shortly after the second change in the slope of the monitored current, which limited the deposition size to approximately 1−2 μm. As shown in Figure S17(c), the Au deposition undergoes dendrite-type growth. The produced dendrites are important because their sizes are below the critical size of 60 nm for HR−TEM. Limiting the overall deposition to a size below 60 nm was also attempted; however, it was not feasible to obtain such small deposits at the CNEs. Therefore, the Au dendrite structure was selected for the HR−TEM thickness-dependent stability studies of electrodeposited Ir. In Figure S17(d), the electrochemical response of the Au UME exhibits typical Au UME characteristics, such as the Au oxidation and Au_{ox} reduction peaks (further discussion in Supporting Information, Part V. Identical Location TEM Analysis: Preparation of Ir films with different thicknesses).

4.6.3. Single Cell Operation. Multielectrode arrays (MEAs) were fabricated by sandwiching the ED Ir/Pt/Ti electrode, a Nafion membrane coated with Pt/C on the other side, and a C PTL (10 BC, SIGRACET) in sequence. Nafion 115 with 0.4 mg_{Pt} cm^{-2} Pt/C was used as a membrane and cathode catalyst for the evaluation of the performance and stability during the long-term single cell tests. Pt/C was spray-coated onto the membrane surface from a slurry composed of Pt/C (46.9 wt %, Tanaka), a Nafion ionomer solution, isopropyl alcohol, and deionized water. The ionomer content of the Pt catalyst layer was 30 wt %. The MEAs were hot-pressed at 43.6 MPa for 1 min and assembled between Ti and C bipolar plates (serpentine flow-field, torque: 9.0 N m). Spray-coated Ir(IV) oxide (99.99% (metals basis), Alfa−Aesar) on the anode side of the membrane (1.5 mg_{Ir} cm^{-2}, 10 wt % of the Nafion ionomer) assembled with a Ti PTL (c-IrO_x) was used for a comparison with the ED Ir electrodes. The cells used in this study resembled cells reported elsewhere;[76,77] however, instead of using a current collector, the bipolar plates were directly connected (see also Figure S8).

During the single cell measurements, deionized water was supplied (flow rate: 15 mL min^{-1}) only through the anode. The temperature of both the water and cell during the operation was 80 °C. IV curves were obtained in a voltage range from 1.25 to 2.0 V at a scan rate of 10 mV s^{-1} using a high-current potentiostat (HCP-803; Bio-Logic). To conduct IV measurements before and after long-term operation including *iR* correction, the current was measured at each voltage for 1 min from 1.25 to 2.0 V with an interval of 0.05 V. During the long-term operation, the following measurements were repeated from (i) to (iii): (i) from 0.1 and 0.2 to 2.0 A cm^{-2} with an 0.2 A cm^{-2} interval during 1.5 s at each current, (ii) 0.1 A cm^{-2} for 6.0 h, and (iii) 2.0 A cm^{-2} for 6.0 h. During 6 h of each constant-current operation, the HFR value was measured at 10 kHz every 10 min to obtain the *iR*-corrected voltage for the long-term operation. Before and after the long-term operation, LSV (from 0.05 to 0.8 V, scan rate: 2 mV s^{-1}) and CV (from 0.05 to 0.6, 1.1, and 1.4 V, scan rate: 20 mV s^{-1}) measurements were conducted in a fully humidified environment, with N_2 purged at the anode and H_2 purged at the anode, respectively (further discussion in Supporting Information, Part III: Proton-exchange Membrane Water Electrolysis).

ASSOCIATED CONTENT

Supporting Information

The Supporting Information is available free of charge at https://pubs.acs.org/doi/10.1021/acscatal.4c07864.

Additional experimental details, including photographs of the experimental setup, methods, and discussion (PDF)

AUTHOR INFORMATION

Corresponding Authors

Ioannis Spanos − *Department of Heterogeneous Reactions, Max Planck Institute for Chemical Energy Conversion (MPI-CEC), 45470 Mülheim an der Ruhr, Germany;* orcid.org/0000-0001-5737-4992; Email: ioannis.spanos@cec.mpg.de

Hyun S. Park − *Center for Hydrogen Fuel Cell Research, Korea Institute of Science and Technology, Seoul 02792, Republic of Korea;* orcid.org/0000-0002-7960-9729; Email: hspark@kist.re.kr

Authors

Ahyoun Lim − *Center for Hydrogen Fuel Cell Research, Korea Institute of Science and Technology, Seoul 02792, Republic of Korea; Department of Heterogeneous Reactions, Max Planck Institute for Chemical Energy Conversion (MPI-CEC), 45470 Mülheim an der Ruhr, Germany*

Kahyun Ham − *Department of Heterogeneous Reactions, Max Planck Institute for Chemical Energy Conversion (MPI-CEC), 45470 Mülheim an der Ruhr, Germany*

Thomas Quast − *Analytical Chemistry—Center for Electrochemical Sciences (CES), Faculty of Chemistry and Biochemistry, Ruhr University Bochum, D-44780 Bochum, Germany*

Suji Lee − *Center for Hydrogen Fuel Cell Research, Korea Institute of Science and Technology, Seoul 02792, Republic of Korea; School of Chemical and Biological Engineering, Seoul National University, Seoul 08826, Republic of Korea*

Marc F. Tesch − *Department of Heterogeneous Reactions, Max Planck Institute for Chemical Energy Conversion (MPI-CEC), 45470 Mülheim an der Ruhr, Germany*
Steffen Czioska − *Institute for Chemical Technology and Polymer Chemistry and Institute of Catalysis Research and Technology, Karlsruhe Institute of Technology, 76131 Karlsruhe, Germany*
Daniela Ramermann − *Department of Heterogeneous Reactions, Max Planck Institute for Chemical Energy Conversion (MPI-CEC), 45470 Mülheim an der Ruhr, Germany*
Walid Hetaba − *Department of Heterogeneous Reactions, Max Planck Institute for Chemical Energy Conversion (MPI-CEC), 45470 Mülheim an der Ruhr, Germany;* orcid.org/0000-0003-4728-0786
Wolfgang Schuhmann − *Analytical Chemistry—Center for Electrochemical Sciences (CES), Faculty of Chemistry and Biochemistry, Ruhr University Bochum, D-44780 Bochum, Germany;* orcid.org/0000-0003-2916-5223
Jan-Dierk Grunwaldt − *Institute for Chemical Technology and Polymer Chemistry and Institute of Catalysis Research and Technology, Karlsruhe Institute of Technology, 76131 Karlsruhe, Germany;* orcid.org/0000-0003-3606-0956
Sung Ki Cho − *Center for Hydrogen Fuel Cell Research, Korea Institute of Science and Technology, Seoul 02792, Republic of Korea;* orcid.org/0000-0002-5173-8625
Hee-Young Park − *Center for Hydrogen Fuel Cell Research, Korea Institute of Science and Technology, Seoul 02792, Republic of Korea*
Jong Hyun Jang − *Center for Hydrogen Fuel Cell Research, Korea Institute of Science and Technology, Seoul 02792, Republic of Korea*
Sang Hyun Ahn − *Department of Chemical Engineering, Chung-Ang University, Seoul 06974, Republic of Korea;* orcid.org/0000-0001-8906-5908

Complete contact information is available at:
https://pubs.acs.org/10.1021/acscatal.4c07864

Funding

Open access funded by Max Planck Society.

Funding

This work was supported by the National Research Foundation of Korea (RS-2024−00466554), the Ministry of Trade, Industry and Energy of Korea (20223030040220), and the Korea Institute of Science and Technology. A.L., K.H., I.S., T.Q., and W.S. are grateful for the funding provided through the German BMBF cluster projects "DERIEL" (FKZ 03HY122I and 03HY122H).

Notes

The authors declare no competing financial interest.

■ ACKNOWLEDGMENTS

The authors would like to acknowledge DESY (Hamburg, Germany), a member of the Helmholtz Association HGF, for providing the experimental facilities. Parts of this research were conducted at PETRA III, and the authors would like to thank Wolfgang Caliebe and Aleksandr Kalinko for their assistance with using the quick EXAFS setup at beamline P64. The beam time was allocated for proposal I-20221226. The authors would like to thank Norbert Pfänder for the TEM measurements and interpretation.

■ REFERENCES

(1) Dvorak, M. T.; Armour, K. C.; Frierson, D. M. W.; Proistosescu, C.; Baker, M. B.; Smith, C. J. Estimating the timing of geophysical commitment to 1.5 and 2.0 °C of global warming. *Nat. Clim. Change* **2022**, *12* (6), 547−552.

(2) Doo, G.; Park, J.; Park, J.; Heo, J.; Jung, J.; Lee, D. W.; Bae, H.; Hyun, J.; Oh, E.; Kwen, J.; Kim, K. M.; Kim, H.-T. Contact Problems of IrOx Anodes in Polymer Electrolyte Membrane Water Electrolysis. *ACS Energy Lett.* **2023**, *8* (5), 2214−2220.

(3) Park, J. E.; Kim, S.; Kim, O.-H.; Ahn, C.-Y.; Kim, M.-J.; Kang, S. K.; Jeon, T., Il; Shim, J.-E.; Lee, D. W.; Lee, J. H.; Cho, Y.-H.; Sung, Y.-E. Ultra-low loading of IrO2 with an inverse-opal structure in a polymer-exchange membrane water electrolysis. *Nano Energy* **2019**, *58*, 158−166.

(4) Kim, Y. J.; Lim, A.; Kim, J. M.; Lim, D.; Chae, K. H.; Cho, E. N.; Han, H. J.; Jeon, K. U.; Kim, M.; Lee, G. H.; Lee, G. R.; Ahn, H. S.; Park, H. S.; Kim, H.; Kim, J. Y.; Jung, Y. S. Highly efficient oxygen evolution reaction via facile bubble transport realized by three-dimensionally stack-printed catalysts. *Nat. Commun.* **2020**, *11* (1), No. 4921.

(5) Oh, J. H.; Han, G. H.; Kim, H.; Jang, H. W.; Park, H. S.; Kim, S. Y.; Ahn, S. H. Activity and stability of Ir-based gas diffusion electrode for proton exchange membrane water electrolyzer. *Chem. Eng. J.* **2021**, *420*, No. 127696.

(6) Faustini, M.; Giraud, M.; Jones, D.; Rozière, J.; Dupont, M.; Porter, T. R.; Nowak, S.; Bahri, M.; Ersen, O.; Sanchez, C.; Boissière, C.; Tard, C.; Peron, J. Hierarchically Structured Ultraporous Iridium-Based Materials: A Novel Catalyst Architecture for Proton Exchange Membrane Water Electrolyzers. *Adv. Energy Mater.* **2019**, *9* (4), No. 1802136.

(7) Yu, H.; Bonville, L.; Jankovic, J.; Maric, R. Microscopic insights on the degradation of a PEM water electrolyzer with ultra-low catalyst loading. *Appl. Catal., B* **2020**, *260*, No. 118194.

(8) Zhao, S.; Stocks, A.; Rasimick, B.; More, K.; Xu, H. Highly Active, Durable Dispersed Iridium Nanocatalysts for PEM Water Electrolyzers. *J. Electrochem. Soc.* **2018**, *165* (2), No. F82.

(9) Claudel, F.; Dubau, L.; Berthomé, G.; Sola-Hernandez, L.; Beauger, C.; Piccolo, L.; Maillard, F. Degradation Mechanisms of Oxygen Evolution Reaction Electrocatalysts: A Combined Identical-Location Transmission Electron Microscopy and X-ray Photoelectron Spectroscopy Study. *ACS Catal.* **2019**, *9* (5), 4688−4698.

(10) Feng, Q.; Yuan, X. Z.; Liu, G.; Wei, B.; Zhang, Z.; Li, H.; Wang, H. A review of proton exchange membrane water electrolysis on degradation mechanisms and mitigation strategies. *J. Power Sources* **2017**, *366*, 33−55.

(11) Alia, S. M.; Rasimick, B.; Ngo, C.; Neyerlin, K. C.; Kocha, S. S.; Pylypenko, S.; Xu, H.; Pivovar, B. S. Activity and Durability of Iridium Nanoparticles in the Oxygen Evolution Reaction. *J. Electrochem. Soc.* **2016**, *163* (11), No. F3105.

(12) Chandesris, M.; Médeau, V.; Guillet, N.; Chelghoum, S.; Thoby, D.; Fouda-Onana, F. Membrane degradation in PEM water electrolyzer: Numerical modeling and experimental evidence of the influence of temperature and current density. *Int. J. Hydrogen Energy* **2015**, *40* (3), 1353−1366.

(13) Wang, Z. B.; Hu, H. X.; Liu, C. B.; Zheng, Y. G. The effect of fluoride ions on the corrosion behavior of pure titanium in 0.05M sulfuric acid. *Electrochim. Acta* **2014**, *135*, 526−535.

(14) Toops, T. J.; Brady, M. P.; Zhang, F.-Y.; Meyer, H. M.; Ayers, K.; Roemer, A.; Dalton, L. Evaluation of nitrided titanium separator plates for proton exchange membrane electrolyzer cells. *J. Power Sources* **2014**, *272*, 954−960.

(15) Rakousky, C.; Keeley, G. P.; Wippermann, K.; Carmo, M.; Stolten, D. The stability challenge on the pathway to high-current-density polymer electrolyte membrane water electrolyzers. *Electrochim. Acta* **2018**, *278*, 324−331.

(16) Sun, S.; Shao, Z.; Yu, H.; Li, G.; Yi, B. Investigations on degradation of the long-term proton exchange membrane water electrolysis stack. *J. Power Sources* **2014**, *267*, 515−520.

(17) Lettenmeier, P.; Wang, R.; Abouatallah, R.; Helmly, S.; Morawietz, T.; Hiesgen, R.; Kolb, S.; Burggraf, F.; Kallo, J.; Gago, A. S.; Friedrich, K. A. Durable Membrane Electrode Assemblies for Proton Exchange Membrane Electrolyzer Systems Operating at High Current Densities. *Electrochim. Acta* **2016**, *210*, 502−511.

(18) Rakousky, C.; Reimer, U.; Wippermann, K.; Carmo, M.; Lueke, W.; Stolten, D. An analysis of degradation phenomena in polymer electrolyte membrane water electrolysis. *J. Power Sources* **2016**, *326*, 120−128.

(19) Rakousky, C.; Reimer, U.; Wippermann, K.; Kuhri, S.; Carmo, M.; Lueke, W.; Stolten, D. Polymer electrolyte membrane water electrolysis: Restraining degradation in the presence of fluctuating power. *J. Power Sources* **2017**, *342*, 38−47.

(20) Grigoriev, S. A.; Bessarabov, D. G.; Fateev, V. N. Degradation mechanisms of MEA characteristics during water electrolysis in solid polymer electrolyte cells. *Russ. J. Electrochem.* **2017**, *53* (3), 318−323.

(21) Yu, H.; Danilovic, N.; Wang, Y.; Willis, W.; Poozhikunnath, A.; Bonville, L.; Capuano, C.; Ayers, K.; Maric, R. Nano-size IrOx catalyst of high activity and stability in PEM water electrolyzer with ultra-low iridium loading. *Appl. Catal., B* **2018**, *239*, 133−146.

(22) Weiß, A.; Siebel, A.; Bernt, M.; Shen, T. H.; Tileli, V.; Gasteiger, H. A. Impact of Intermittent Operation on Lifetime and Performance of a PEM Water Electrolyzer. *J. Electrochem. Soc.* **2019**, *166* (8), No. F487.

(23) Suermann, M.; Bensmann, B.; Hanke-Rauschenbach, R. Degradation of Proton Exchange Membrane (PEM) Water Electrolysis Cells: Looking Beyond the Cell Voltage Increase. *J. Electrochem. Soc.* **2019**, *166* (10), No. F645.

(24) Papakonstantinou, G.; Algara-Siller, G.; Teschner, D.; Vidaković-Koch, T.; Schlögl, R.; Sundmacher, K. Degradation study of a proton exchange membrane water electrolyzer under dynamic operation conditions. *Appl. Energy* **2020**, *280*, No. 115911.

(25) Ferner, K. J.; Park, J.; Kang, Z.; Mauger, S. A.; Ulsh, M.; Bender, G.; Litster, S. Morphological analysis of iridium oxide anode catalyst layers for proton exchange membrane water electrolysis using high-resolution imaging. *Int. J. Hydrogen Energy* **2024**, *59*, 176−186.

(26) Weber, C. C.; De Angelis, S.; Meinert, R.; Appel, C.; Holler, M.; Guizar-Sicairos, M.; Gubler, L.; Büchi, F. N. Microporous transport layers facilitating low iridium loadings in polymer electrolyte water electrolysis. *EES Catal.* **2024**, *2* (2), 585−602.

(27) Cherevko, S. Stability and dissolution of electrocatalysts: Building the bridge between model and "real world" systems. *Curr. Opin. Electrochem.* **2018**, *8*, 118−125.

(28) Ahn, S. H.; Tan, H.; Haensch, M.; Liu, Y.; Bendersky, L. A.; Moffat, T. P. Self-terminated electrodeposition of iridium electrocatalysts. *Energy Environ. Sci.* **2015**, *8* (12), 3557−3562.

(29) Tanuma, S.; Powell, C. J.; Penn, D. R. Calculations of electron inelastic mean free paths. V. Data for 14 organic compounds over the 50−2000 eV range. *Surf. Interface Anal.* **1994**, *21* (3), 165−176.

(30) Lim, A.; Kim, J.; Lee, H. J.; Kim, H.-J.; Yoo, S. J.; Jang, J. H.; Young Park, H.; Sung, Y.-E.; Park, H. S. Low-loading IrO2 supported on Pt for catalysis of PEM water electrolysis and regenerative fuel cells. *Appl. Catal., B* **2020**, *272*, No. 118955.

(31) Nong, H. N.; Reier, T.; Oh, H.-S.; Gliech, M.; Paciok, P.; Vu, T. H. T.; Teschner, D.; Heggen, M.; Petkov, V.; Schlögl, R.; Jones, T.; Strasser, P. A unique oxygen ligand environment facilitates water oxidation in hole-doped IrNiOx core−shell electrocatalysts. *Nat. Catal.* **2018**, *1* (11), 841−851.

(32) Abbott, D. F.; Lebedev, D.; Waltar, K.; Povia, M.; Nachtegaal, M.; Fabbri, E.; Copéret, C.; Schmidt, T. J. Iridium Oxide for the Oxygen Evolution Reaction: Correlation between Particle Size, Morphology, and the Surface Hydroxo Layer from Operando XAS. *Chem. Mater.* **2016**, *28* (18), 6591−6604.

(33) Fabbri, E.; Abbott, D. F.; Nachtegaal, M.; Schmidt, T. J. Operando X-ray absorption spectroscopy: A powerful tool toward water splitting catalyst development. *Curr. Opin. Electrochem.* **2017**, *5* (1), 20−26.

(34) Henke, B. L.; Gullikson, E. M.; Davis, J. C. X-Ray Interactions: Photoabsorption, Scattering, Transmission, and Reflection at E = 50−30,000 eV, Z = 1−92. *At. Data Nucl. Data Tables* **1993**, *54* (2), 181−342.

(35) King, H. J.; Fournier, M.; Bonke, S. A.; Seeman, E.; Chatti, M.; Jumabekov, A. N.; Johannessen, B.; Kappen, P.; Simonov, A. N.; Hocking, R. K. Photon-Induced, Timescale, and Electrode Effects Critical for the in Situ X-ray Spectroscopic Analysis of Electrocatalysts: The Water Oxidation Case. *J. Phys. Chem. C* **2019**, *123* (47), 28533−28549.

(36) Binninger, T.; Fabbri, E.; Patru, A.; Garganourakis, M.; Han, J.; Abbott, D. F.; Sereda, O.; Kötz, R.; Menzel, A.; Nachtegaal, M.; Schmidt, T. J. Electrochemical Flow-Cell Setup for In Situ X-ray Investigations. *J. Electrochem. Soc.* **2016**, *163* (10), No. H906.

(37) Caliebe, W. A.; Murzin, V.; Kalinko, A.; Görlitz, M. In *High-Flux XAFS-Beamline P64 at PETRA III*, AIP Conference Proceedings; AIP, 2019; p 060031.

(38) Bornmann, B.; Kläs, J.; Müller, O.; Lützenkirchen-Hecht, D.; Frahm, R. In *The Quick EXAFS Setup at Beamline P64 at PETRA III for up to 200 Spectra Per Second*, AIP Conference Proceedings; AIP, 2019; p 040008.

(39) Czioska, S.; Ehelebe, K.; Geppert, J.; Escalera-López, D.; Boubnov, A.; Saraçi, E.; Mayerhöfer, B.; Krewer, U.; Cherevko, S.; Grunwaldt, J. D. Heating up the OER: Investigation of IrO2 OER Catalysts as Function of Potential and Temperature. *ChemElectroChem* **2022**, *9* (19), No. e202200514.

(40) Pfeifer, V.; Jones, T. E.; Velasco Velez, J. J.; Massue, C.; Greiner, M. T.; Arrigo, R.; Teschner, D.; Girgsdies, F.; Scherzer, M.; Allan, J.; Hashagen, M.; Weinberg, G.; Piccinin, S.; Havecker, M.; Knop-Gericke, A.; Schlogl, R. The electronic structure of iridium oxide electrodes active in water splitting. *Phys. Chem. Chem. Phys.* **2016**, *18* (4), 2292−2296.

(41) van der Merwe, M.; Wibowo, R. E.; Jimenez, C. E.; Escudero, C.; Agostini, G.; Bär, M.; Garcia-Diez, R. Electronic and Structural Property Comparison of Iridium-Based OER Nanocatalysts Enabled by Operando Ir L3-Edge X-ray Absorption Spectroscopy. *ACS Catal.* **2024**, *14* (22), 16759−16769.

(42) Nattino, F.; Marzari, N. Operando XANES from first-principles and its application to iridium oxide. *Phys. Chem. Chem. Phys.* **2020**, *22* (19), 10807−10818.

(43) Danilovic, N.; Subbaraman, R.; Chang, K. C.; Chang, S. H.; Kang, Y. J.; Snyder, J.; Paulikas, A. P.; Strmcnik, D.; Kim, Y. T.; Myers, D.; Stamenkovic, V. R.; Markovic, N. M. Activity-Stability Trends for the Oxygen Evolution Reaction on Monometallic Oxides in Acidic Environments. *J. Phys. Chem. Lett.* **2014**, *5* (14), 2474−2478.

(44) Bizzotto, F.; Quinson, J.; Zana, A.; Kirkensgaard, J. J. K.; Dworzak, A.; Oezaslan, M.; Arenz, M. Ir nanoparticles with ultrahigh dispersion as oxygen evolution reaction (OER) catalysts: synthesis and activity benchmarking. *Catal. Sci. Technol.* **2019**, *9* (22), 6345−6356.

(45) Minguzzi, A.; Lugaresi, O.; Achilli, E.; Locatelli, C.; Vertova, A.; Ghigna, P.; Rondinini, S. Observing the oxidation state turnover in heterogeneous iridium-based water oxidation catalysts. *Chem. Sci.* **2014**, *5* (9), 3591−3597.

(46) Pfeifer, V.; Jones, T. E.; Velez, J. J. V.; Arrigo, R.; Piccinin, S.; Havecker, M.; Knop-Gericke, A.; Schlogl, R. In situ observation of reactive oxygen species forming on oxygen-evolving iridium surfaces. *Chem. Sci.* **2017**, *8* (3), 2143−2149.

(47) Mom, R. V.; Falling, L. J.; Kasian, O.; Algara-Siller, G.; Teschner, D.; Crabtree, R. H.; Knop-Gericke, A.; Mayrhofer, K. J. J.; Velasco-Vélez, J.-J.; Jones, T. E. Operando Structure−Activity−Stability Relationship of Iridium Oxides during the Oxygen Evolution Reaction. *ACS Catal.* **2022**, *12* (9), 5174−5184.

(48) Foucher, A. C.; Rosen, D. J.; Yang, S.; Ferreira Sanchez, D.; Sadykov, I.; Grolimund, D.; Frenkel, A. I.; Murray, C. B.; Stach, E. A. Stable and Efficient Ir Nanoshells for Oxygen Reduction and Evolution Reactions. *Chem. Mater.* **2023**, *35* (11), 4572−4580.

(49) Siracusano, S.; Baglio, V.; Grigoriev, S. A.; Merlo, L.; Fateev, V. N.; Aricò, A. S. The influence of iridium chemical oxidation state on

the performance and durability of oxygen evolution catalysts in PEM electrolysis. *J. Power Sources* **2017**, *366*, 105−114.

(50) Li, T.; Kasian, O.; Cherevko, S.; Zhang, S.; Geiger, S.; Scheu, C.; Felfer, P.; Raabe, D.; Gault, B.; Mayrhofer, K. J. J. Atomic-scale insights into surface species of electrocatalysts in three dimensions. *Nat. Catal.* **2018**, *1* (4), 300−305.

(51) Knöppel, J.; Mockl, M.; Escalera-Lopez, D.; Stojanovski, K.; Bierling, M.; Bohm, T.; Thiele, S.; Rzepka, M.; Cherevko, S. On the limitations in assessing stability of oxygen evolution catalysts using aqueous model electrochemical cells. *Nat. Commun.* **2021**, *12* (1), No. 2231.

(52) El-Sayed, H. A.; Weiß, A.; Olbrich, L. F.; Putro, G. P.; Gasteiger, H. A. OER Catalyst Stability Investigation Using RDE Technique: A Stability Measure or an Artifact? *J. Electrochem. Soc.* **2019**, *166* (8), F458−F464.

(53) Tang, H.; Qi, Z.; Ramani, M.; Elter, J. F. PEM fuel cell cathode carbon corrosion due to the formation of air/fuel boundary at the anode. *J. Power Sources* **2006**, *158* (2), 1306−1312.

(54) Zhang, S.; Yuan, X.-Z.; Hin, J. N. C.; Wang, H.; Wu, J.; Friedrich, K. A.; Schulze, M. Effects of open-circuit operation on membrane and catalyst layer degradation in proton exchange membrane fuel cells. *J. Power Sources* **2010**, *195* (4), 1142−1148.

(55) Siracusano, S.; Trocino, S.; Briguglio, N.; Pantò, F.; Aricò, A. S. Analysis of performance degradation during steady-state and load-thermal cycles of proton exchange membrane water electrolysis cells. *J. Power Sources* **2020**, *468*, No. 228390, DOI: 10.1016/j.jpowsour.2020.228390.

(56) Grigoriev, S. A.; Dzhus, K. A.; Bessarabov, D. G.; Millet, P. Failure of PEM water electrolysis cells: Case study involving anode dissolution and membrane thinning. *Int. J. Hydrogen Energy* **2014**, *39* (35), 20440−20446.

(57) Fouda-Onana, F.; Chandesris, M.; Médeau, V.; Chelghoum, S.; Thoby, D.; Guillet, N. Investigation on the degradation of MEAs for PEM water electrolysers part I: Effects of testing conditions on MEA performances and membrane properties. *Int. J. Hydrogen Energy* **2016**, *41* (38), 16627−16636.

(58) Kasian, O.; Grote, J. P.; Geiger, S.; Cherevko, S.; Mayrhofer, K. J. J. The Common Intermediates of Oxygen Evolution and Dissolution Reactions during Water Electrolysis on Iridium. *Angew. Chem., Int. Ed.* **2018**, *57* (9), 2488−2491.

(59) Reier, T.; Pawolek, Z.; Cherevko, S.; Bruns, M.; Jones, T.; Teschner, D.; Selve, S.; Bergmann, A.; Nong, H. N.; Schlogl, R.; Mayrhofer, K. J.; Strasser, P. Molecular Insight in Structure and Activity of Highly Efficient, Low-Ir Ir-Ni Oxide Catalysts for Electrochemical Water Splitting (OER). *J. Am. Chem. Soc.* **2015**, *137* (40), 13031−13040.

(60) Massué, C.; Pfeifer, V.; van Gastel, M.; Noack, J.; Algara-Siller, G.; Cap, S.; Schlogl, R. Reactive Electrophilic O(I-) Species Evidenced in High-Performance Iridium Oxohydroxide Water Oxidation Electrocatalysts. *ChemSusChem* **2017**, *10* (23), 4786−4798.

(61) Saveleva, V. A.; Wang, L.; Teschner, D.; Jones, T.; Gago, A. S.; Friedrich, K. A.; Zafeiratos, S.; Schlogl, R.; Savinova, E. R. Operando Evidence for a Universal Oxygen Evolution Mechanism on Thermal and Electrochemical Iridium Oxides. *J. Phys. Chem. Lett.* **2018**, *9* (11), 3154−3160.

(62) Lettenmeier, P.; Wang, L.; Golla-Schindler, U.; Gazdzicki, P.; Canas, N. A.; Handl, M.; Hiesgen, R.; Hosseiny, S. S.; Gago, A. S.; Friedrich, K. A. Nanosized IrO(x)-Ir Catalyst with Relevant Activity for Anodes of Proton Exchange Membrane Electrolysis Produced by a Cost-Effective Procedure. *Angew. Chem., Int. Ed.* **2016**, *55* (2), 742−746.

(63) Lee, S. W.; Baik, C.; Kim, D.-H.; Pak, C. Control of Ir oxidation states to overcome the trade-off between activity and stability for the oxygen evolution reaction. *J. Power Sources* **2021**, *493*, No. 229689.

(64) Gu, F.; Zheng, L.; Wei, H.; Mi, W.; Zhang, C.; Su, Q.; Zhu, W.; Lin, W. Tuning amorphous Ir-IrOx oxygen evolution catalyst via precursor complexation for efficient and durable water electrolysis. *Appl. Surf. Sci.* **2022**, *606*, No. 155008.

(65) Baik, C.; Lee, S. W.; Pak, C. Glycine-induced ultrahigh-surface-area IrO2@IrOx catalyst with balanced activity and stability for efficient water splitting. *Electrochim. Acta* **2021**, *390*, No. 138885.

(66) Chatterjee, S.; Peng, X.; Intikhab, S.; Zeng, G.; Kariuki, N. N.; Myers, D. J.; Danilovic, N.; Snyder, J. Nanoporous Iridium Nanosheets for Polymer Electrolyte Membrane Electrolysis. *Adv. Energy Mater.* **2021**, *11* (34), No. 2101438.

(67) Islam, J.; Kim, S.-K.; Thien, P. T.; Kim, M.-J.; Cho, H.-S.; Cho, W.-C.; Kim, C.-H.; Lee, C.; Lee, J. H. Enhancing the activity and durability of iridium electrocatalyst supported on boron carbide by tuning the chemical state of iridium for oxygen evolution reaction. *J. Power Sources* **2021**, *512*, No. 230506.

(68) Mirshekari, G.; Ouimet, R.; Zeng, Z.; Yu, H.; Bliznakov, S.; Bonville, L.; Niedzwiecki, A.; Capuano, C.; Ayers, K.; Maric, R. High-performance and cost-effective membrane electrode assemblies for advanced proton exchange membrane water electrolyzers: Long-term durability assessment. *Int. J. Hydrogen Energy* **2021**, *46* (2), 1526−1539.

(69) Dong, S.; Zhang, C.; Yue, Z.; Zhang, F.; Zhao, H.; Cheng, Q.; Wang, G.; Xu, J.; Chen, C.; Zou, Z.; Dou, Z.; Yang, H. Overall Design of Anode with Gradient Ordered Structure with Low Iridium Loading for Proton Exchange Membrane Water Electrolysis. *Nano Lett.* **2022**, *22* (23), 9434−9440.

(70) Ding, L.; Wang, W.; Xie, Z.; Li, K.; Yu, S.; Capuano, C. B.; Keane, A.; Ayers, K.; Zhang, F. Y. Highly Porous Iridium Thin Electrodes with Low Loading and Improved Reaction Kinetics for Hydrogen Generation in PEM Electrolyzer Cells. *ACS Appl. Mater. Interfaces* **2023**, *15* (20), 24284−24295.

(71) Xie, Z.; Ding, L.; Yu, S.; Wang, W.; Capuano, C. B.; Keane, A.; Ayers, K.; Cullen, D. A.; Meyer, H. M.; Zhang, F.-Y. Ionomer-free nanoporous iridium nanosheet electrodes with boosted performance and catalyst utilization for high-efficiency water electrolyzers. *Appl. Catal., B* **2024**, *341*, No. 123298.

(72) Bernt, M.; Siebel, A.; Gasteiger, H. A. Analysis of Voltage Losses in PEM Water Electrolyzers with Low Platinum Group Metal Loadings. *J. Electrochem. Soc.* **2018**, *165* (5), F305−F314.

(73) Müller, O. Hard X-ray Synchrotron Beamline Instrumentation for Millisecond Quick Extended X-ray Absorption Spectroscopy, P.hD. Thesis; Universität Wuppertal, 2016.

(74) Ravel, B.; Newville, M. ATHENA, ARTEMIS, HEPHAESTUS: data analysis for X-ray absorption spectroscopy using IFEFFIT. *J. Synchrotron Radiat.* **2005**, *12* (4), 537−541.

(75) Wilde, P.; Quast, T.; Aiyappa, H. B.; Chen, Y. T.; Botz, A.; Tarnev, T.; Marquitan, M.; Feldhege, S.; Lindner, A.; Andronescu, C.; Schuhmann, W. Towards Reproducible Fabrication of Nanometre-Sized Carbon Electrodes: Optimisation of Automated Nanoelectrode Fabrication by Means of Transmission Electron Microscopy. *ChemElectroChem* **2018**, *5* (20), 3083−3088.

(76) Rho, K. H.; Na, Y.; Ha, T.; Kim, D. K. Performance Analysis of Polymer Electrolyte Membrane Water Electrolyzer Using OpenFOAM((R)): Two-Phase Flow Regime, Electrochemical Model. *Membranes* **2020**, *10* (12), No. 441, DOI: 10.3390/membranes10120441.

(77) Liu, C.; Wippermann, K.; Rasinski, M.; Suo, Y.; Shviro, M.; Carmo, M.; Lehnert, W. Constructing a Multifunctional Interface between Membrane and Porous Transport Layer for Water Electrolyzers. *ACS Appl. Mater. Interfaces* **2021**, *13* (14), 16182−16196.